

# Molecular clouds: do they deserve a non-Gaussian description?

Pablo Richard<sup>1</sup>, Erwan Allys<sup>1</sup>, François Levrier<sup>1</sup>, Antoine Gusdorf<sup>1,2</sup>, Constant Auclair<sup>1</sup>

<sup>1</sup> Laboratoire de Physique de l'École normale supérieure, ENS, Université PSL, CNRS, Sorbonne Université, Université Paris Cité, Paris, France

<sup>2</sup> Observatoire de Paris, Université PSL, Sorbonne Université, LERMA, CNRS UMR 8112, 75014 Paris, France

Submitted to A&A on July 13, 2024.

## ABSTRACT

Molecular clouds are astrophysical objects whose complex non-linear dynamics is reflected in their complex morphological features. Many studies, investigating the bridge between higher-order statistics and physical properties, have shown the interest provided by non-Gaussian morphological features to grasp physical information. Yet, as this bridge is usually characterized in the supervised world of simulations, transferring it onto observations can be hazardous, especially when the discrepancy between simulations and observations remains unknown. In this paper, we aim at evaluating, directly from the observation data, the discriminating ability of a set of statistics. To do so, we develop a test that allows to compare, for a given unlabeled dataset, the informative power of two sets of summary statistics, relying on a notion of statistical compatibility. Contrary to supervised approaches, this test does not require the knowledge of any class or parameter corresponding to the data, but focuses instead on comparing the degeneracy levels of these descriptors, relying on a notion of statistical compatibility. We apply this test to column density maps of 14 nearby molecular clouds observed by *Herschel*, and iteratively compare different sets of usual summary statistics. We show that a standard Gaussian description of these clouds is highly degenerate but can be substantially improved when being estimated on the logarithm of the maps. This illustrates that low-order statistics, properly used, remain a very powerful tool. We then further show that such descriptions still exhibit a small quantity of degeneracies, some of which are lifted by the higher order statistics provided by reduced wavelet scattering transforms. This property of observations quantitatively differs from state-of-the-art simulations of dense molecular cloud collapse and is not reproduced by log fractional Brownian motion models. Finally we show how the summary statistics identified can be cooperatively used to build a morphological distance, which is evaluated visually, and gives very satisfactory results.

**Key words.** ISM: clouds – ISM: structure – Submillimeter: ISM – Methods: statistical

## 1. Introduction

Molecular clouds (MCs) play a key role in star formation. Their highly non-linear dynamics tends to couple spatial scales over a wide range, to create dense filamentary structures, in which clumps form that will eventually lead to prestellar cores (McKee & Ostriker 2007). However, the precise role of each physical ingredient (such as turbulence, magnetic fields, and gravity, to name but a few) in this dynamics still remains to be fully understood.

A key step towards such an understanding certainly resides in our ability to decipher, in the morphology of these structured clouds, some signature of the physical processes at play. For instance, the power-law shape of the power spectrum in emission maps may trace properties of the turbulence (Miville-Deschênes et al. (2007); Federrath & Klessen (2013)), or the shape of the probability distribution function (PDF) of column density maps (Vázquez-Semadeni et al. 1997; Hennebelle & Chabrier 2008; Kainulainen et al. 2009; Federrath & Klessen 2013; Schneider et al. 2022; Appel et al. 2022) may trace the impact of gravitational collapse or stellar feedback as it transitions from a log-normal shape to the development of a heavy tail.

However, the strong non-linear interplay between the physical processes at work leads to the emergence of non-Gaussian features in interstellar structures, such as filaments. This has motivated numerous studies to capture physical information beyond one-point and two-point statistics. Many approaches have been

investigated including, for instance, diagnostics of the phase coherence of the Fourier modes (Levrier et al. 2006; Burkhardt & Lazarian 2016), bispectrum (Burkhardt et al. 2009), structure functions (Heyer & Brunt 2004), dendograms (Goodman et al. 2009), multiscale segmentation (Robitaille et al. 2019), scattering transforms (Allys et al. 2019; Regalado-Saint Blancard et al. 2020; Saydjari et al. 2021), and neural networks (Peek & Burkhardt 2019; Zavagno et al. 2023).

If higher-order statistics represent an appealing way of refining the geometrical description of complex ISM structures, they are nevertheless subject to the following caveats:

1. They should not screen out the potential of low-order statistics, but should come as complementary diagnostics (Burkhardt & Lazarian 2016). Low-order descriptors should not be underestimated: it is not because the processes under study are highly non-Gaussian that low-order statistics are only marginally informative. Yet, in numerous studies, such easy-access information is not considered, or even intentionally discarded<sup>1</sup>, to emphasize the contribution of high-order statistics.
2. Refining the statistical description with higher-order terms complicates the connection between the statistical descriptions and the physical processes and associated parameters. Such a connection is thus usually learned in the supervised world of simulations, but transferring it to observations can

<sup>1</sup> The mean and variance of the data may be normalized, the power spectra flattened, and histograms (non-linearly) equalized.

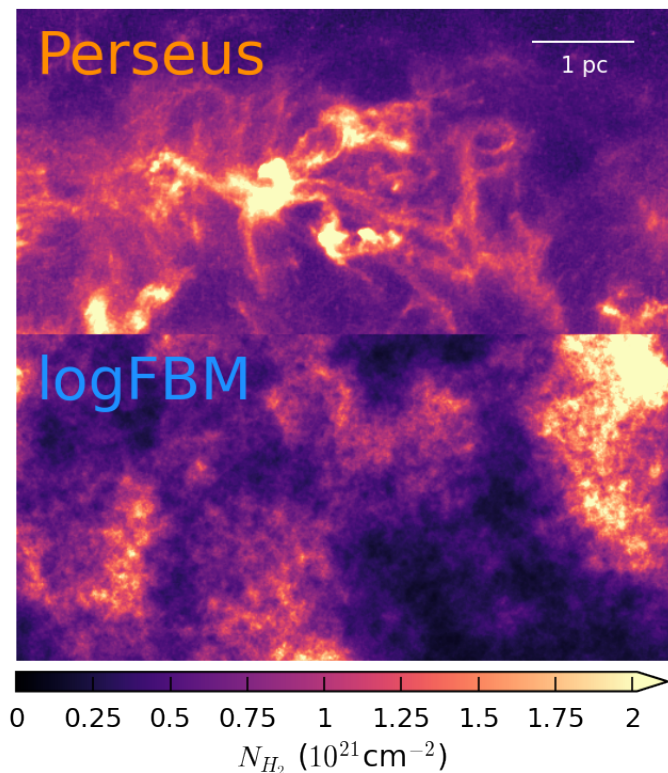


**Fig. 1.** Column density map of a region in Perseus (*top row*) and sample of a log-Fractional Brownian Motion field (*bottom row*). Each image has  $256 \times 512$  pixels but is tiled into 2 complementary patches of size  $256 \times 256$  on which the statistics shown in Fig. 2 are computed. While these one-point and two-point statistics (some being non-Gaussian) are clearly compatible, these two images have manifestly different morphologies.

be hazardous, especially when their distance to simulations remains unknown (Falgarone et al. 2004; Peek & Burkhardt 2019).

In this paper, we aim at identifying what sets of summary statistics are relevant to characterize the diversity of observed molecular clouds, without relying on simulations nor prior knowledge. In such an unsupervised framework, various observations cannot be grouped *a priori* in a similar class, so one often has to work in a very low data regime, which restricts dramatically the range of tools that can be used. This unsupervised and prior-knowledge free framework excludes features that require significant tuning to extract information, such as neural networks. This priority shift, from theoretical informativeness to actual information retrievable in this framework, might reshuffle the cards among the various sets of summary statistics to consider. This leads us to wonder to what extent non-Gaussian statistics can actually bring meaningful contributions in a fully observation-driven and unsupervised framework.

To answer this question, we rely on a dataset of column density maps constructed from a survey of nearby molecular clouds. Our approach is to identify the amount of degeneracy that a set of summary statistics can have on this dataset, *i.e.*, finding a pair of maps in this dataset that are compatible according to these statistics, but actually have a different morphology. A simplified illustration of such a degeneracy is given in Figs. 1 and 2, where we compare an observed column density map with a realization of a field whose logarithm is sampled from a Fractional Brownian

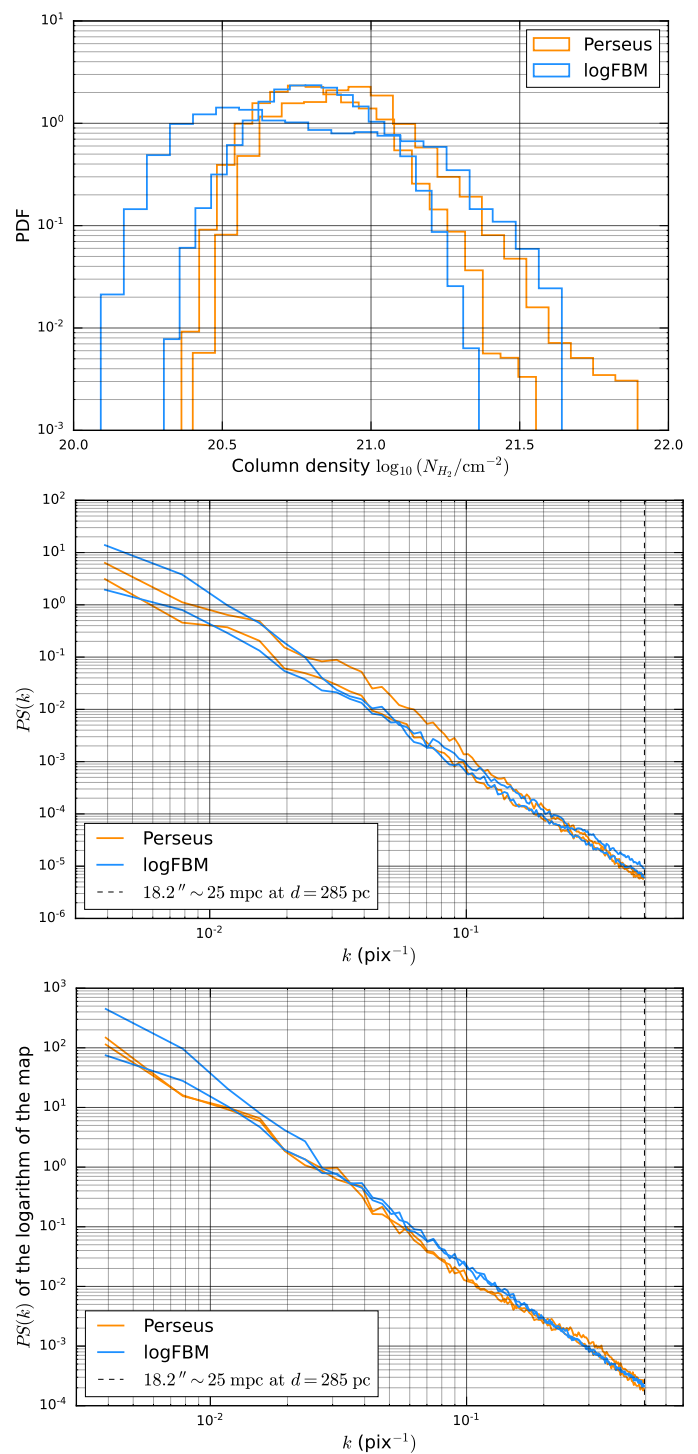


**Fig. 2.** Statistical properties of the maps from Fig. 1: PDFs (*top*), power spectra (*center*), and power spectra of the logarithms of the maps (*bottom*). The dashed vertical line in the power spectra plots is located at the  $18.2''$  resolution of the column density map from the observational dataset. Power spectra are apodized as explained in Sec. 4. We see that the logFBM process is compatible with this observed portion of MC for all these statistics (some of them being non-Gaussian), while having a manifestly different morphology, as revealed in Fig. 1. All these statistics are thus degenerate for such a comparison.

Motion, that is a specific type of Gaussian process with power-law type constrained power spectrum. In this example, the PDFs of these maps, their power spectra, and the power spectra of their

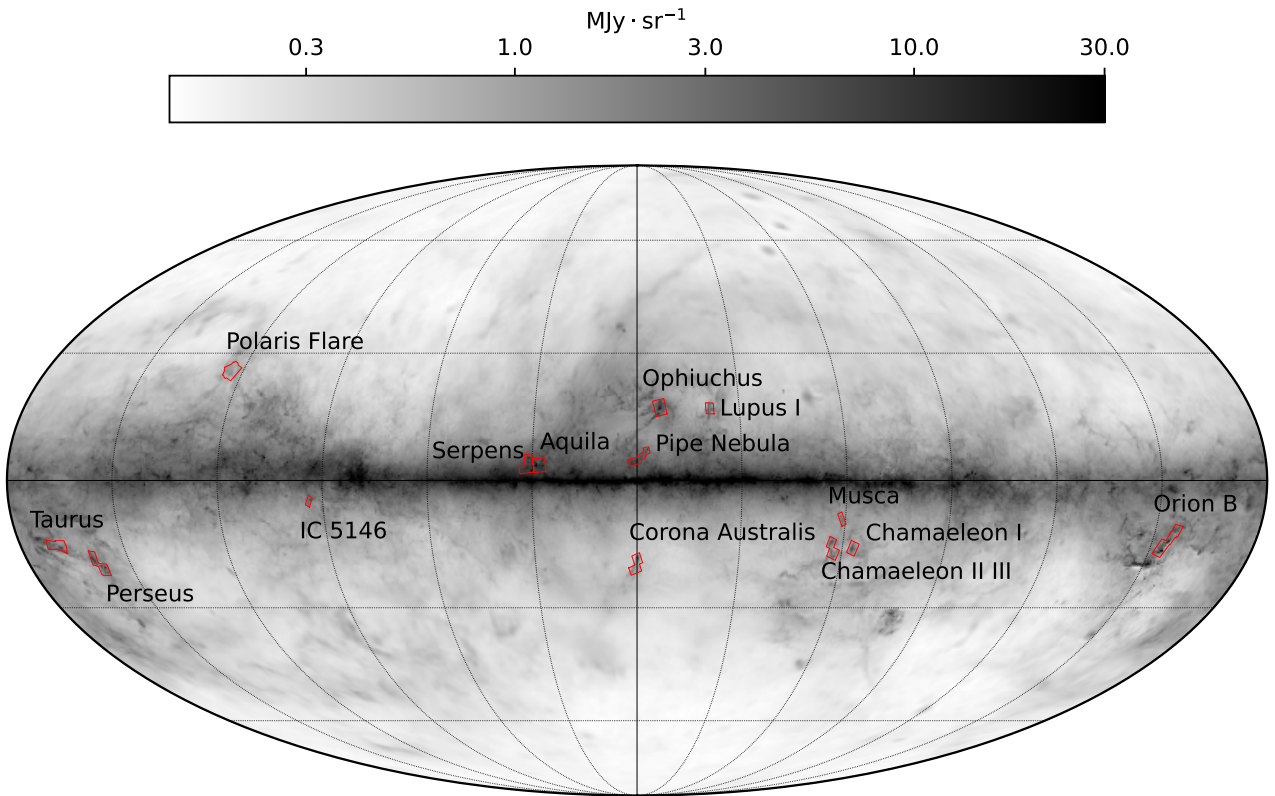


**Fig. 3.** Footprints of the *Herschel* Gould Belt Survey (HGBS) fields used in this study, overlaid on the total thermal dust intensity at 353 GHz from the GNILC (Remazeilles et al. 2011) variable resolution data of *Planck* (Planck Collaboration 2020).

logarithms, all seem to be compatible, even though the maps clearly have different structures. This illustration underlines the limitation of those statistics, but only for this specific comparison, where we compare one observation to a specific known model. However, in an unsupervised framework, when working solely with unlabeled observations, we will exhibit these limitations by introducing additional statistics that could be used to lift these degeneracies.

In this work, we use such a degeneracy diagnostic on the observed molecular clouds dataset to progressively build a robust set of summary statistics. We start with basic statistics, such as the power spectrum and one-point statistics. We evidence strong limitations that we investigate and substantially mitigate by taking the logarithm of the maps beforehand. We evidence further but moderate limitations of this improved set, leveraging higher-order statistics through the reduced wavelet scattering transform (RWST). This study, initially carried out only on the observational dataset, is then extended to logFBM data, as well as to a set of magnetohydrodynamics (MHD) simulations intended to reproduce observations of dense star-forming molecular clouds. We conclude by discussing the relevance and limitations of the final set of statistics we have constructed, and show how it can be used to assess the distance, in a statistical sense, between different maps of the interstellar medium.

The structure of the paper is as follows:

- In section 2, we present the set of MCs considered in this work and the corresponding column density maps, as well as the numerical simulations and the logFBM models.

- We present in section 3 the diagnostic of statistical compatibility that we will rely on, and our general methodology.
- We present in section 4 the sets of statistics that will be confronted.
- We apply this methodology in section 5 to confront these sets of statistics on observations, and from these results we design an informative and low-dimensional set of summary statistics  $\phi_{\text{final}}$ .
- We finally define, in section 6, a distance based on  $\phi_{\text{final}}$  that allows us to compare datasets, such as observations and simulations.

## 2. Data

In this section, we present the main dataset that we use for this study: an ensemble of  $\sim 550$  molecular hydrogen ( $\text{H}_2$ ) column density maps from a survey of nearby molecular clouds (MCs). Three other datasets will be used in this paper:

- a set of  $\sim 230$  total gas column density maps built from magnetohydrodynamical (MHD) numerical simulations of dense molecular clouds, classified into three subsets with varying values of the magnetic field, from null (*hydro*), to medium (*MHD*), and high (*MHD high B*). These simulations are state-of-the-art attempts to reproduce the physics at play in the early stages of star formation, including self-gravity and decaying turbulence, and are therefore well adapted to compare to our observations of the HGBS clouds.

- A set of  $\sim 500$  synthetic maps sampled from logFBM models, whose parameters reproduce the diversity of the observational dataset. This type of purely synthetic fields has already been extensively used to model the interstellar medium (see, e.g., Elmegreen 2002; Brunt & Heyer 2002; Miville-Deschênes et al. 2007; Levrier et al. 2018).
- A set of  $\sim 1000$  images from a large collection of everyday textures, the Describable Texture Dataset (DTD, Cimpoi et al. (2014)). We use these to emphasize the specificity of ISM fields in the context of image texture analysis.

More details about these sets are given in appendix A. All these maps have a size of  $512 \times 512$  pixels.

### 2.1. Observations: column density maps from the HGBS

We focus our study on a set of MCs targeted by the Gould Belt Survey (HGBS) (André et al. 2010) with the *Herschel* Space Observatory (Pilbratt et al. 2010), whose footprints on the sky are shown in Fig. 3. The HGBS combines two main criteria we require for this work:

- it sampled numerous MCs with a diversity of physical and environmental conditions, from diffuse and quiescent regions with no sign of star-formation activity such as the Polaris Flare (Heithausen & Thaddeus 1990; André et al. 2010; Miville-Deschênes et al. 2010) to very dense and active ones such as Orion B (Schneider et al. 2013) or the Aquila Rift cloud (Könyves et al. 2015). Examples of molecular column density maps from the HGBS are shown in Fig. 4. We however emphasize that this survey is limited to local clouds (distances  $d \leq 500$  pc) and does not cover the whole range of conditions expected in Galactic molecular clouds<sup>2</sup>.
- It imaged a broad range of scales, from the full cloud size ( $\sim 10$  pc, corresponding to a few degrees for these nearby clouds) down to the  $\sim 0.1$  pc scales of filaments (Arzoumanian et al. 2011; André et al. 2014), which are spatially resolved for the nearest clouds<sup>3</sup>, thus covering more than 2 orders of magnitude in spatial scales. This allows us to perform an in-depth morphological analysis, based on a local description of multi-scale interactions.

We consider the high resolution ( $18''$ ) column density maps of 14 regions, produced with the procedure described in Appendix A of Palmeirim et al. (2013) and publicly available from the *Herschel* Gould Belt Survey Archive<sup>4</sup>. This  $18''$  angular resolution corresponds to a 12 mpc spatial resolution for the nearest clouds, such as Ophiuchus and Taurus ( $d \sim 140$  pc), and up to 40 mpc for the most distant clouds, such as Orion B ( $d \sim 450$  pc). The main properties of these clouds are given in Table 1.

### 2.2. Subsampling and tiling

The presence of physical processes such as gravity in the dynamics of MCs implies spatial variations of their statistical properties, which prevents us from modeling them as stationary stochastic processes. For instance, they usually have strong local overdensities, while being surrounded by diffuse borders. This

<sup>2</sup> A further study could target more distant, more massive star forming regions with interferometric observations. We postpone such a study to a future paper.

<sup>3</sup> The typical resolutions range from  $10''$  at  $70 \mu\text{m}$  to  $36''$  at  $500 \mu\text{m}$ .

<sup>4</sup> [http://www.herschel.fr/cea/gouldbelt/en/Phocaea/Vie\\_des\\_labos/Ast/\ast\\_visu.php?id\\_ast=66](http://www.herschel.fr/cea/gouldbelt/en/Phocaea/Vie_des_labos/Ast/\ast_visu.php?id_ast=66)

non-homogeneity makes it difficult to compare such objects as a whole, as well as to properly estimate their statistical properties, when seen as realizations of a random process, as these properties will for instance depend heavily on the identification of the cloud boundary, or on the precise definition of what a cloud is. Furthermore, variance estimates for random processes generally rely on a homogeneity assumption to estimate the intrinsic variability of a process from its spatial variations. More broadly, the estimation of the statistical moments and properties of a process is usually based on spatial averaging, which assumes the homogeneity of the sample.

To avoid this problem, we choose to restrict the comparison to local patches of these MCs, assuming statistical homogeneity within each individual patch. This requires the identification of a characteristic stationarity length over which it can be assumed that the statistical properties of the cloud do not vary significantly. Different patches extracted from the same cloud may have different statistical properties, which will be representative of the non-homogeneity of the cloud as a whole. This encourages us to use small patches. However, an additional difficulty is that these patches must be large enough to make statistical estimates. In particular, variance estimates require sampling beyond the correlation length of the process under study.

In this paper, we have chosen to cut patches with angular sizes ranging from  $0.85^\circ$  to  $2.55^\circ$ , that correspond respectively to 3 pc and 9 pc for a cloud at a typical distance of 200 pc. We believe this represents a good compromise with regard to the trade-off expressed above. However, we are aware that there may not be an ideal solution, especially as we have no precise estimate of neither the stationarity length nor the correlation length. This means that we cannot rule out some confusion between local intrinsic variability and large-scale variations in the statistical properties of the clouds. However, we believe that, for lack of a better solution, this does not undermine the relevance of this study.

More precisely, we make multiple versions of the original ( $18''$  resolution,  $3''$  pixel size) column density maps at different pixel sizes ( $6''$ ,  $9''$ ,  $12''$ , and  $18''$ ). The down-sampling is done using a bivariate spline approximation of order 3 of the original maps. Then, we cut from these maps patches of size in pixels  $512 \times 512$ , with a step size of 256 pixels, such that two neighboring patches will have 50% of their pixels in common. In the following, these patches will be themselves tiled into 4 sub patches of size  $256 \times 256$  to perform a variability estimation. The choice of  $6''$  for the finest sampling allows us to exploit the  $18''$  resolution of these maps with mitigated sampling artifacts. The  $9''$ ,  $12''$ , and  $18''$  pixel sizes respectively correspond to a relative shrinking of the  $6''$  pixel maps with ratios of 1.5, 2, and 3, which allows to accommodate for the significant and quite uncertain range of distances of the different MCs in the HGBS. This entire procedure, which is illustrated in Fig. 5, and summarized in Table 1, leads to a total of 551 patches with size  $512 \times 512$  pixels, each of which is then subdivided into four  $256 \times 256$  sub-patches.

## 3. Quantifying informative power of summary statistics on an unlabeled dataset

### 3.1. General methodology

We want to quantify the amount of information we can exploit from a given set of summary statistics on a given dataset. However, because we work with unlabeled data, we cannot use supervised frameworks, such as Fisher analysis, that have a label-

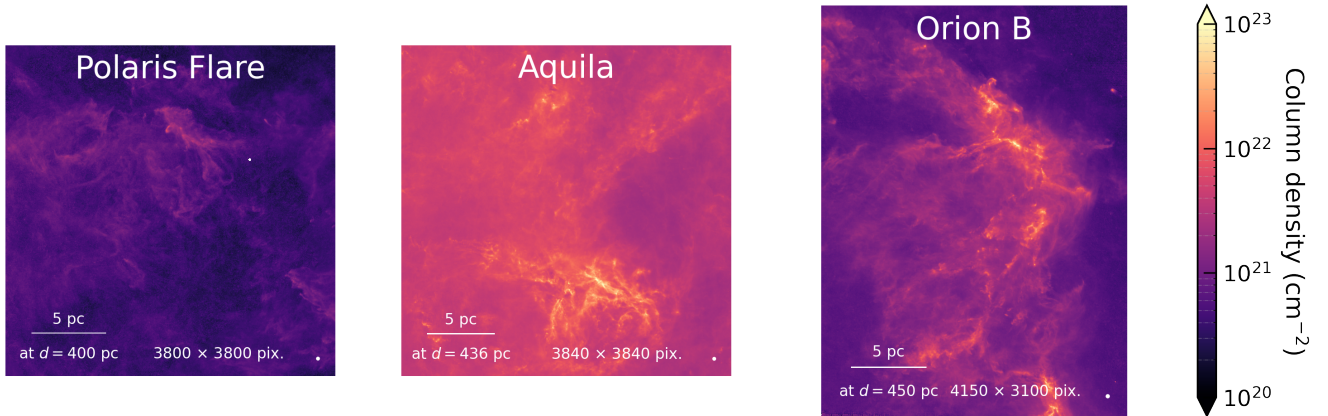


**Fig. 4.** Column density maps of three regions from the HGBS. The spatial resolution of the maps is  $18''$ , sampled with a pixel size of  $3''$ . A white dot with diameter  $5 \times 18''$  is shown at the bottom right corner of each map. Estimates of spatial scales, also shown on the maps, are based on reported distances (see Table 1). The Polaris Flare is an example of a diffuse and quiescent cloud, while Aquila and Orion B are dense and very active star-forming regions.

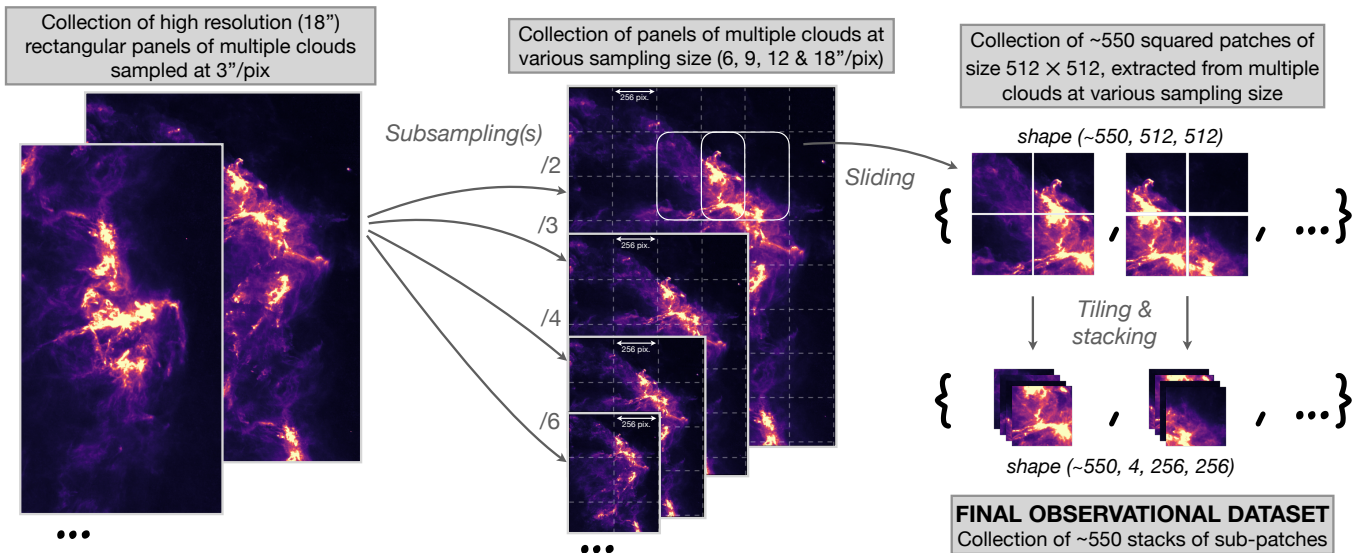


**Fig. 5.** Illustration of the pre-processing of observational data. Details are given in Sec. 2.2.

based approach to quantify information. For instance, when working with simulations, each sampled data  $x_i$  can be labeled by its corresponding physical parameters  $\theta_i$ . In our case, we have to deal with an ensemble of unlabeled maps, for which we have *a priori* no notion of distance between pairs.

In this paper, we choose to rely on a notion of compatibility between patches, that can be estimated for any set of summary statistics. This approach allows to be quantitative, even in this unsupervised setting. Nevertheless, without supervision, it remains difficult to interpret a compatibility result between two patches for a given set of summary statistics: do the two patches actually have very similar properties, or do they have very dis-

tinct properties whose differences are not effectively caught by the statistics?

This difficulty can be partially overcome by using complementary sets of statistics. Indeed, if two patches are distinguished by a first set of statistics, this is sufficient to assess that they are in practice different, and therefore to highlight the degeneracies of another set of statistics. It is this comparative approach, which is all the more relevant when the panel of statistics compared is comprehensive, that we use in this paper.

The informative power of a set of statistics strongly depends on the family of processes studied. For instance, we know that the empirical mean and power spectrum are sufficient statistics for stationary Gaussian fields (Cover 1999), which is not the case

Region	Dist. $d$ (pc)	Coord.		# patches with resolution					References
		$l$ (°)	$b$ (°)	Tot.	6"	9"	12"	18"	
Aquila	436	28	4	57	36	16	4	1	Ortiz-León et al. (2018)
Chamaeleon I	210	296	-16	28	20	6	2	0	Zucker et al. (2020)
Chamaeleon II III	160	302	-16	43	32	8	3	0	Zucker et al. (2020)
Corona Australis	160	0	-19	44	34	7	3	0	Zucker et al. (2020)
IC 5146	750	94	-5	4	4	0	0	0	Zucker et al. (2020)
Lupus I	182	339	17	17	12	4	1	0	Galli et al. (2013)
Musca	200	301	-9	6	6	0	0	0	Knude & Hog (1998)
Ophiuchus	139	353	17	61	42	12	6	1	Mamajek (2008)
Orion B	450	205	-14	88	61	19	7	1	Schlafly et al. (2014); Zucker et al. (2020)
Perseus	285	159	-20	44	32	10	2	0	Zucker et al. (2020)
Pipe Nebula	180	359	6	23	18	5	0	0	Zucker et al. (2020)
Polaris Flare	400	123	26	50	36	9	4	1	Schlafly et al. (2014); Zucker et al. (2020)
Serpens	436	31	4	46	33	9	4	0	Ortiz-León et al. (2018)
Taurus	145	170	-16	40	30	6	4	0	Yan et al. (2019)

**Table 1.** Summary of the properties of the different MCs studied in this paper, as well as their division into patches at different sampling. References in the rightmost column are for the distance estimates, which can be quite uncertain (uncertainties are given in the references quoted).

for physical processes in general. In this paper, we will apply our approach to the dataset of observations defined above, as well as to numerical simulations and synthetic logFBM models. In addition, we note that this diagnostic can also be used to compare maps from two different datasets.

In the rest of this section, we introduce the compatibility criterion, and explain how we extend it from a pair level to a dataset level. The set of statistics used in this paper will be presented in the following section.

### 3.2. Statistical compatibility for a pair of patches

We want to measure a notion of compatibility, according to a given set of summary statistics  $\phi$ , between the two processes that generated the patches  $(x_i, x_j)$ . To estimate this  $\phi$ -compatibility, we need to make a number of simplifications, given the low-data regime, which will bring us back to a simplified case of statistical hypothesis testing. To do so, we tile each patch  $x_i$  into 4 sub patches  $\{x_i^{(l)}\}_{1 \leq l \leq 4}$ , as illustrated in Fig. 5. We then compute the statistics at this sub patch level:  $\{\phi(x_i^{(l)})\}_{1 \leq l \leq 4}$  and we assume that these random variables can be considered as independent samples of the same distribution, that we furthermore model as multivariate normal distribution<sup>5</sup> of mean  $\mu_i$  and variance  $\Sigma_i$ :

$$\phi(x_i^{(l)}) \sim \mathcal{N}(\mu_i, \Sigma_i). \quad (1)$$

Under these assumptions, the problem boils down to testing the compatibility between the two normal distributions, *i.e.*, to test the hypothesis:  $\mu_i = \mu_j$  and  $\Sigma_i = \Sigma_j$ . In our case, however, we have to estimate this compatibility from very few samples, most of the time fewer than the dimension of the vector of statistics  $\phi$ . We thus choose to focus only on testing if the means  $\mu_i$  and  $\mu_j$  are statistically compatible, but not  $\Sigma_i$  and  $\Sigma_j$ , a problem known as the *multivariate two-sample mean test*. The most widespread test statistic for this problem is the Hotelling's two-sample  $T^2$ -statistic, a multivariate extension of Student's  $t$ -test (Hotelling

<sup>5</sup> This assumption is not far from being true when the law of large numbers can be applied to the distribution of  $\phi(x)$ . This is for instance the case when  $\phi(x)$  is defined as an average over the image pixels of a certain local distortion (such as filtering, possibly non linear)  $\phi_{loc}(x)$  of  $x$ :  $\phi(x) = \langle \phi_{loc}(x) | \mathbf{u} \rangle_{\mathbf{u}}$  and when the process  $\phi_{loc}(x)$  is stationary with a correlation length that is small compared to the image length.

1931). However, this test statistic requires to invert an estimation  $S$  of the full covariance matrix  $\Sigma_i + \Sigma_j$ , which is usually intractable in our low data regime.

To overcome this, Srivastava & Du (2008) proposed a test statistic based only on the diagonal  $D_S$  of the covariance estimator  $S$ , and on the trace of the square of its associated correlation matrix  $R \equiv D_S^{-1/2} S D_S^{-1/2}$ :

$$d_{\phi}^2(x_i, x_j) \equiv \alpha \left[ (\hat{\mu}_i - \hat{\mu}_j)^T D_S^{-1} (\hat{\mu}_i - \hat{\mu}_j) - \beta \right], \quad (2)$$

where  $\hat{\mu}_i$  is the estimator of  $\mu_i$  obtained through an average over the 4 sub-patches  $x_i^{(l)}$ ,  $\alpha$  is an overall factor to normalize the variance of  $d_{\phi}^2$ , and  $\beta$  is a debiasing term. We emphasize that, through a dependence on  $tr(R^2)$ , the  $\alpha$  factor accounts, at least partially, for the correlation structure of  $\phi$ . More details about these terms are given in appendix C.

Under the assumption that  $\Sigma_i = \Sigma_j$ , the  $d_{\phi}^2(x_i, x_j)$  test statistic has a variance of order unity. Thus, when it is much larger than 1,  $\mu_i$  &  $\mu_j$  cannot be considered compatible:

$$d_{\phi}^2(x_i, x_j) \gg 1 \implies \mu_i \text{ \& \ } \mu_j \text{ incompatible}, \quad (3)$$

whereas when it is of the order of 1 or less, it is not possible to detect a discrepancy between the two means  $\mu_i$  and  $\mu_j$  with the available amount of data:

$$d_{\phi}^2(x_i, x_j) \lesssim 1 \implies \mu_i \text{ \& \ } \mu_j \text{ not incompatible based on the available amount of data.} \quad (4)$$

### 3.3. Comparing summary statistics on a dataset

By extending the  $\phi$ -compatibility test introduced above, we set up a comparison between two sets of summary statistics  $\phi_A$  and  $\phi_B$  on a given dataset. This comparison consists in studying whether each set of summary statistics has degeneracies that the other set can lift. These degeneracies are evidenced by the presence in the dataset of pairs of maps that are clearly incompatible for  $\phi_A$ , but for which  $\phi_B$  detects no incompatibility, or *vice versa*. To be relevant, this comparison requires that the dataset contain maps that actually have different properties, which will be the case for the data sets studied later.

In practice, we suggest the following algorithm:

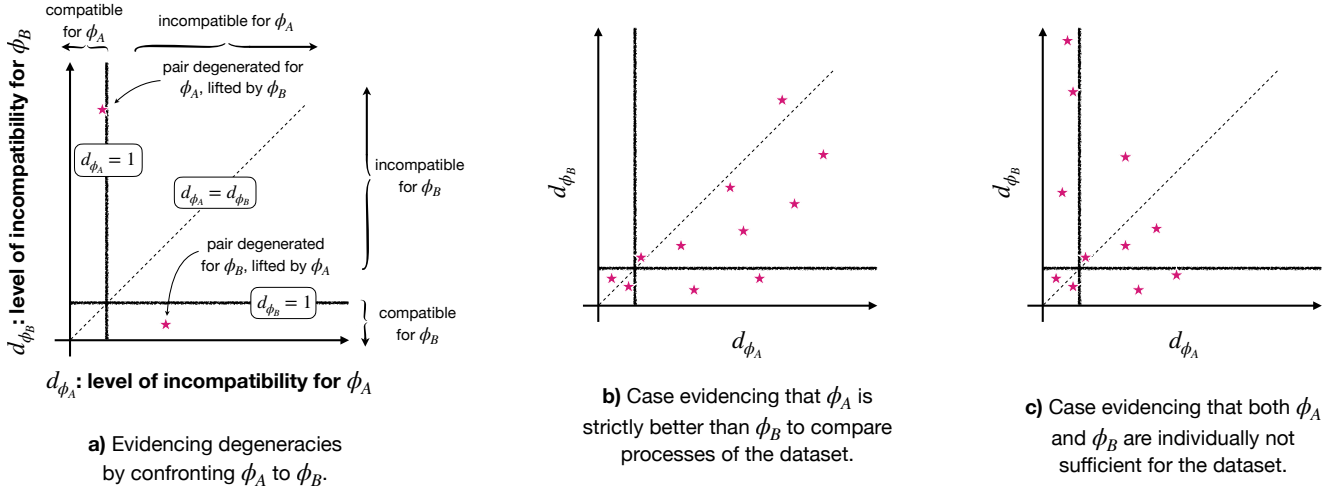


**Fig. 6.** Illustration of the proposed test to confront two sets of summary statistics,  $\phi_A$  vs  $\phi_B$ , on their degeneracy level for a given dataset. Each star represents a pair of patches. Panel a: the presence of stars in the bottom right region, *i.e.*, where  $d_{\phi_A} \gg 1$  and  $d_{\phi_B} \lesssim 1$ , reveals that some pairs of this dataset are identified by  $\phi_A$  as incompatible but not by  $\phi_B$ : such pairs thus evidence degeneracies of  $\phi_B$  lifted by  $\phi_A$ . Conversely, the presence of stars in the top left region evidences degeneracies of  $\phi_A$  lifted by  $\phi_B$ . Hence, if all the points land mainly in the sub-diagonal part (panel b), this evidences that  $\phi_A$  is better suited than  $\phi_B$  to compare the pairs of this dataset. If on the contrary the points are spread both in the upper left and bottom right regions of the plot (panel c), this shows that both  $\phi_A$  and  $\phi_B$  are individually not sufficient to describe the processes of this dataset.

- Step 1: for every patch  $x_i$  of the dataset, compute the statistics  $\phi_A$  and  $\phi_B$  of its corresponding sub-patches  $\{x_i^{(l)}\}_l$ .
- Step 2: for every pair  $\{x_i, x_j\}$  with  $i \neq j$ , compute  $d_{\phi_A}^2(x_i, x_j)$  and  $d_{\phi_B}^2(x_i, x_j)$  from the quantities derived in step 1.
- Step 3: place every pair as a point on a 2D scatter plot showing  $d_{\phi_A}^2(x_i, x_j)$  against  $d_{\phi_B}^2(x_i, x_j)$ , such as Fig. 6.

The resulting scatter plot can then be used to detect whether there are some pairs of processes in the dataset that are degenerate for  $\phi_A$  but lifted by  $\phi_B$  (or *vice versa*), as explained in Fig. 6. In such plots, the presence of points in the bottom right region, *i.e.*, where  $d_{\phi_A} \gg 1$  and  $d_{\phi_B} \lesssim 1$ , reveals that some pairs of this dataset are identified by  $\phi_A$  as incompatible but not by  $\phi_B$ : such pairs thus evidence degeneracies of  $\phi_B$  lifted by  $\phi_A$  (panel a). Conversely, the presence of points in the top left region evidences degeneracies of  $\phi_A$  lifted by  $\phi_B$ . Hence, if all the points land mainly in the sub-diagonal part (panel b), this evidences that  $\phi_A$  is better suited than  $\phi_B$  to compare the pairs of this dataset. If on the contrary the points are spread both in the upper left and bottom right regions of the plot (panel c), this shows that both  $\phi_A$  and  $\phi_B$  are individually not sufficient to describe the processes of this dataset.

## 4. Summary statistics

We present below the different summary statistics that are used in this paper. In the following,  $x$  is an image,  $x(\mathbf{u})$  is the value of the image at pixel  $\mathbf{u}$ ,  $\tilde{x}(\mathbf{k})$  is the discrete Fourier transform of image  $x$  evaluated at wave-vector  $\mathbf{k}$ ,  $\star$  stands for the convolution operator, and  $\langle \cdot \rangle_{\mathbf{u}}$  for the averaging over pixels. When  $\phi(x)$  is multivariate,  $\phi(x)[i]$  is the value of its  $i$ -th dimension.  $\bar{x}$  designates the following normalization of  $x$ :  $\bar{x} \equiv x/\text{std}(x)$  where  $\text{std}(x) \equiv \sqrt{\langle [x - \langle x \rangle_{\mathbf{u}}]^2 \rangle_{\mathbf{u}}}$ .

Note that for some usual statistics, we consider their logarithms instead of their raw values. For instance we use  $\log \langle x \rangle_{\mathbf{u}}$

instead of  $\langle x \rangle_{\mathbf{u}}$ . This is possible when we work with positive-valued statistics. We made this choice to better fit the Gaussianity assumption given Eq. (1). In addition, we found that logarithms expressed more discriminatory power with our diagnostic. See appendix D for more details. If no precision is made, log designates the logarithm in base 10.

### 4.1. One-point based statistics

We list below the one-point statistics used in this paper. Even though some of these statistics can probe non Gaussian information such as sparsity, they are all point wise statistics. This means in particular that they cannot capture spatial arrangement in the maps.

- The mean:

$$\phi_{\text{mean}}(x) \equiv \log \langle x \rangle_{\mathbf{u}}. \quad (5)$$

- The variance:

$$\phi_{\text{var}}(x) \equiv \log \langle [x - \langle x \rangle_{\mathbf{u}}]^2 \rangle_{\mathbf{u}}. \quad (6)$$

- The mean of the logarithm:

$$\phi_{\text{mean of log}}(x) \equiv \langle \log x \rangle_{\mathbf{u}}. \quad (7)$$

- The variance of the logarithm:

$$\phi_{\text{var of log}}(x) \equiv \log \langle [\log x - \langle \log x \rangle_{\mathbf{u}}]^2 \rangle_{\mathbf{u}}. \quad (8)$$

- The quantile functions<sup>6</sup> (QF) normalized by the median:

$$\phi_{\text{QF}}(x)[i] \equiv \log [q_{\alpha_i}(x)/q_{1/2}(x)], \quad (9)$$

<sup>6</sup> We consider quantile functions rather than probability distribution functions, as the difficulty of defining a unique binning range makes comparisons less efficient. Indeed, to define a range in terms of quantiles allows for a natural adaptation to each MCs' regions.

where  $q_\alpha(x)$  designates the  $\alpha$ -quantile of the distribution of values  $\{x(\mathbf{u})\}_u$ . Hence  $q_{1/2}$  stands for the median operator. We consider 10 quantiles  $\{\alpha_i\}_i$  such that  $1 - \alpha_i$  are logarithmically spaced between  $10^{-4}$  and 0.4. Low quantiles are not considered as, for observational data, they are contaminated (Osenskopf-Okada et al. 2016). This logarithmic binning of the high column density values is motivated by the log-normal to power-law behavior of the tail of MCs' PDFs. See for instance Pouteau et al. (2023) and references therein.

#### 4.2. Two-point based statistics

A very popular way to describe spatial properties of a process is through the power spectrum (PS). It is defined as the Fourier transform of the auto-correlation function, and describes the energy distribution scale by scale in the process studied. In this paper, we consider the isotropic PS, defined as:

$$PS[k] \equiv \langle \mathbb{E}[|\tilde{x}(\mathbf{k})|^2] \rangle_{\|\mathbf{k}\|=k}.$$

A power-law behavior  $PS[k] \propto k^{-\beta}$  is expected for fields arising in turbulent MHD (Schekochihin 2022). Thus we adopt a log-log representation, to linearize it and for stability purposes (Bruna & Mallat 2013):

$$\phi_{PS}(x)[i] \equiv \log \langle |x_{\text{apo}} \star \psi_i|^2 \rangle_u, \quad (10)$$

where  $x_{\text{apo}}$  is apodized to mitigate non periodic boundary conditions (PBC) as explained in appendix B. We use 6 band-pass filters  $\{\psi_i\}_{1 \leq i \leq 6}$  defined as:

$$\tilde{\psi}_i[\mathbf{k}] = 1_{\|\mathbf{k}\| \in [k_i, k_{i+1}[},$$

where  $k_i$  is logarithmically spaced between  $k_{\min} = 1/256 \text{ pix}^{-1}$  and  $k_{\max} = 1/4 \text{ pix}^{-1}$ . For the finest maps with pixel size  $6''$ , this  $k_{\max}$  corresponds to a smallest angular scale of  $24''$ , which remains above the  $18''$  resolution of the observations.

Because some MCs tend to have log-normal behavior in their one-point statistics, we also consider PS statistics of the logarithm of the maps:

$$\phi_{PS \text{ of } \log(x)}[i] \equiv \log \langle |(\log x)_{\text{apo}} \star \psi_i|^2 \rangle_u. \quad (11)$$

#### 4.3. Scattering statistics

The Wavelet Scattering Transform (WST) is a set of non-Gaussian descriptors with a hierarchical and multi-scale structure (Bruna & Mallat 2013). It has been shown to be very efficient at describing astrophysical fields (see, for instance, Allys et al. 2019; Saydjari et al. 2021). The usual WST consists in two layers of statistics, the first of which depends on a single scale of length  $\approx 2^j$  pixels with orientation  $\theta$ :

$$S_1(x)[j, \theta] \equiv \langle |x \star \psi_{j,\theta}| \rangle_u.$$

The second layer probes a coupling between two oriented scales  $(j_1, \theta_1)$ , and  $(j_2, \theta_2)$ , with  $j_1 < j_2$ :

$$S_2(x)[j_1, j_2, \theta_1, \theta_2] \equiv \langle \left| |x \star \psi_{j_1, \theta_1}| \star \psi_{j_2, \theta_2} \right| \rangle_u / S_1(x)[j_1, \theta_1].$$

Then, observing that many processes of interest in astrophysics and cosmology exhibit strong regularities in their angular dependencies, Allys et al. (2019) proposed the Reduced WST (RWST): an angular compression of WST statistics for 2D data. We are going to use three of the main descriptors they introduced (we refer to the above reference for more details):

- $S_1^{Iso}$ , a scale-by-scale isotropic descriptor, that we normalize by estimating it on  $\bar{x}$  instead of  $x$ :

$$S_1^{Iso}(x)[j] \equiv \langle \log_2 \langle |\bar{x} \star \psi_{j,\theta}| \rangle_\theta \rangle. \quad (12)$$

Note that it computes a  $L^1$  norm of the filtered field, in contrast with the power spectrum that probes a  $L^2$  norm.

- $S_2^{Iso1}$  and  $S_2^{Iso2}$ , that measure an isotropic coupling between scales and are defined by fitting the following model:

$$\log_2 S_2(x)[j_1, j_2, \theta_1, \theta_2] \approx S_2^{Iso1}(x)[j_1, j_2] + S_2^{Iso2}(x)[j_1, j_2] \cos[2(\theta_2 - \theta_1)].$$

They characterize, respectively, a coupling between non-oriented scales and the relative coupling between parallel and perpendicular scales.

In this paper, we will furthermore compress both  $S_2^{Iso1}$  and  $S_2^{Iso2}$  coefficients that depend on two scales  $(2^{j_1}, 2^{j_2})$  by only keeping their  $j_2 - j_1$  dependency, *i.e.*, a dependency on their ratio, by considering the following average:

$$\langle S_2^{Iso1} \rangle_{j_2 - j_1}(x)[\delta] \equiv \langle S_2^{Iso1}(x)[j_1, j_2] \rangle_{j_2 - j_1 = \delta}, \quad (13)$$

and

$$\langle S_2^{Iso2} \rangle_{j_2 - j_1}(x)[\delta] \equiv \langle S_2^{Iso2}(x)[j_1, j_2] \rangle_{j_2 - j_1 = \delta}. \quad (14)$$

In practice, we consider 4 scales between  $j_{\min} = 2$  and  $j_{\max} = 5$ , which leads to the 3 possible values  $1 \leq \delta \leq 3$  for our reduced  $S_2$  coefficients. We also divide the half-plane  $[0, \pi[$  in 8 different  $\theta$  angles. For the finest maps of pixel size  $6''$ , this  $j_{\min}$  corresponds to a scale of  $24''$  that remains above the  $18''$  resolution of the observations.

For RWST computations, convolutions are done with local wavelets. This allows us to mitigate non PBC after convolution by suitably cropping the corrupted edges, without using apodization. These computations are done with the `pywst`<sup>7</sup> Python package (Regaldo-Saint Blancard et al. 2020).

$\phi$	Dim.	Non-Gaussian	Scale description	Scale interactions
mean	1	×	×	×
var	1	×	×	×
mean of log	1	log-Gauss.	×	×
var of log	1	log-Gauss.	×	×
QF	10	✓	×	×
PS	6	×	✓	×
PS of log	6	log-Gauss.	✓	×
$S_1^{Iso}$	4	✓	✓	×
$\langle S_2^{Iso1} \rangle_{j_2 - j_1}$	3	✓	×	✓
$\langle S_2^{Iso2} \rangle_{j_2 - j_1}$	3	✓	×	✓

**Table 2.** Overview of the sets of summary statistics, their dimensions and properties (whether they are sensitive to non-Gaussianity, provide a multiscale description, and probe couplings between scales).

<sup>7</sup> <https://github.com/bregaldo/pywst>



#### 4.4. Overview

The statistics introduced above are compiled in Table 2. In the following, in addition to the sets of summary statistics defined above, we will also consider some aggregated sets of summary statistics that are made from groups of these building blocks. For instance, we will refer to  $\phi_{\text{Gaussian}}$  statistics to mean the joint set of  $\{\phi_{\text{mean}}, \phi_{\text{var}}, \phi_{\text{PS}}\}$ . These groups are defined in Table 3.

Set of stats.	Composed of	Dim.
Gaussian	mean + PS	7
log-Gaussian	mean of log + PS of log	7
RWST	$S_1^{Iso} + \langle S_2^{Iso1} \rangle_{j_2-j_1} + \langle S_2^{Iso2} \rangle_{j_2-j_1}$	10
final	log-Gaussian, RWST	17

**Table 3.** Aggregated sets of summary statistics used in this work.

### 5. Towards a low-degeneracy set of statistics

We want to construct a set of informative summary statistics for the observational dataset. To do so, we will follow a bottom-up approach, starting with usual low-order statistics, and increasingly trying to improve on them, by exhibiting and lifting potential degeneracies. The underlying idea is that low-order statistics are good candidates to concentrate most of the informative power into a few coefficients. Such a concentration property is of interest, especially as our low data regime prevents us from learning many features. Another benefit of this approach is to first promote simple statistics, and use more elaborate ones only if they add a significant contribution.

#### 5.1. Molecular clouds have Gaussian degeneracies

To begin with, we investigate whether Gaussian statistics (*i.e.* the set made of mean and PS statistics) are degenerate for the observational data. To point out such potential degeneracies, we confront these Gaussian statistics, starting with a low-order non-Gaussian set of statistics, the quantile function QF, using the methodology introduced in Sec. 3.3. As shown in Fig. 7, this first confrontation on observational data already underlines a strong degeneracy level for both Gaussian and QF features, showing that neither statistics is by itself sufficient, according to the compatibility diagnostic we introduced. In particular, the quantile statistics extract a significant amount of information that cannot be efficiently captured by Gaussian statistics.

In addition to this dataset-wide diagnostic, we display in Fig. 8 six randomly picked pairs of  $512 \times 512$  patches degenerate for Gaussian statistics but with increasing QF incompatibility. The locations of these pairs on the scatter plot of Fig. 7 are given there by the red stars. For these six pairs of patches, we show in Fig. 9 the two sets of statistics used in the diagnostic (QF statistics and Gaussian statistics), where the orange filled lines (resp. bands) correspond to the mean (resp. standard deviation) of the statistics computed over the four  $256 \times 256$  sub-patches of the top patch of each pair of Fig. 8, and the corresponding blue lines and areas refer to the bottom patch of the pair. To better highlight the discrepancies between the two patches of a given pair, the offsets of the orange and blue filled lines with respect to their common mean are also shown in Fig. 9. These results illustrate the ability of QF statistics to distinguish between images with the same Gaussian statistics, which confirms that our compatibility diagnostic works as expected. We emphasize here that

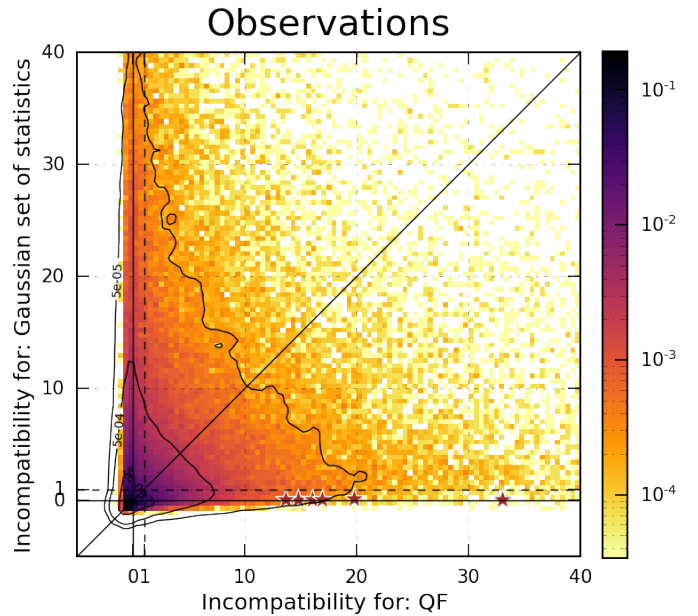


**Fig. 7.** Confronting Gaussian statistics with QF statistics on observational data, based on the test presented in Fig. 6. Each set of statistics has strong degeneracies lifted by the other set. To investigate the Gaussian confusions, we pick six pairs of  $512 \times 512$  patches, whose locations on the scatter plot are given by the red stars. These pairs are shown in Fig. 8.

the  $\phi_{\text{QF}}$  statistics are complementary to the one-point properties probed by Gaussian statistics.

This behavior is not particularly surprising as one-point properties of column density maps of MCs are expected to be at least log-normal, if not with a power-law tail. Hence, estimating such properties directly from the logarithm of the maps, as does  $\phi_{\text{QF}}$  but not  $\phi_{\text{Gaussian}}$ , might enhance the discriminative power. To test this idea, we study in the first column of Fig. 10 the degeneracy level of the set of mean and variance statistics estimated respectively on the raw maps and their logarithm. More precisely, top row plots confront QF statistics to  $\{\phi_{\text{mean}}, \phi_{\text{var}}\}$ , while bottom row plots confront QF statistics to  $\{\phi_{\text{mean of log}}, \phi_{\text{var of log}}\}$ . We see in this figure that the pairs of observations are clearly better discriminated when using the mean and variance computed on the logarithm of the maps (d) rather than directly (a). This effect is very well reproduced by logFBM data (middle column), but does not hold in general, as shown with the Describable Textures Dataset (DTD) (right column).

These results suggest that the specific Gaussian degeneracies evidenced in Fig. 7 are mainly explained by the inefficiency of Gaussian one-point statistics  $\{\phi_{\text{mean}}, \phi_{\text{var}}\}$  to characterize one-point properties of processes that have a log-normal (or heavier tail) nature.

Surprisingly, this analysis also shows that, for datasets such as observations or logFBMs, probing the PDF properties through the prism of a mean and a variance is more discriminative than probing its shape. Here, in both d) and e), our suitably constructed set  $\{\phi_{\text{mean of log}}, \phi_{\text{var of log}}\}$ , of dimension 2, performs almost always a better discrimination than the set  $\phi_{\text{QF}}$ , of dimension 10. This emphasizes the importance of suitably constructed low dimensional descriptions in such analysis. The performative power of such low-dimensional features is usually due to the exploitation of underlying regularities of the studied processes that allow these compression, without much loss of information. For

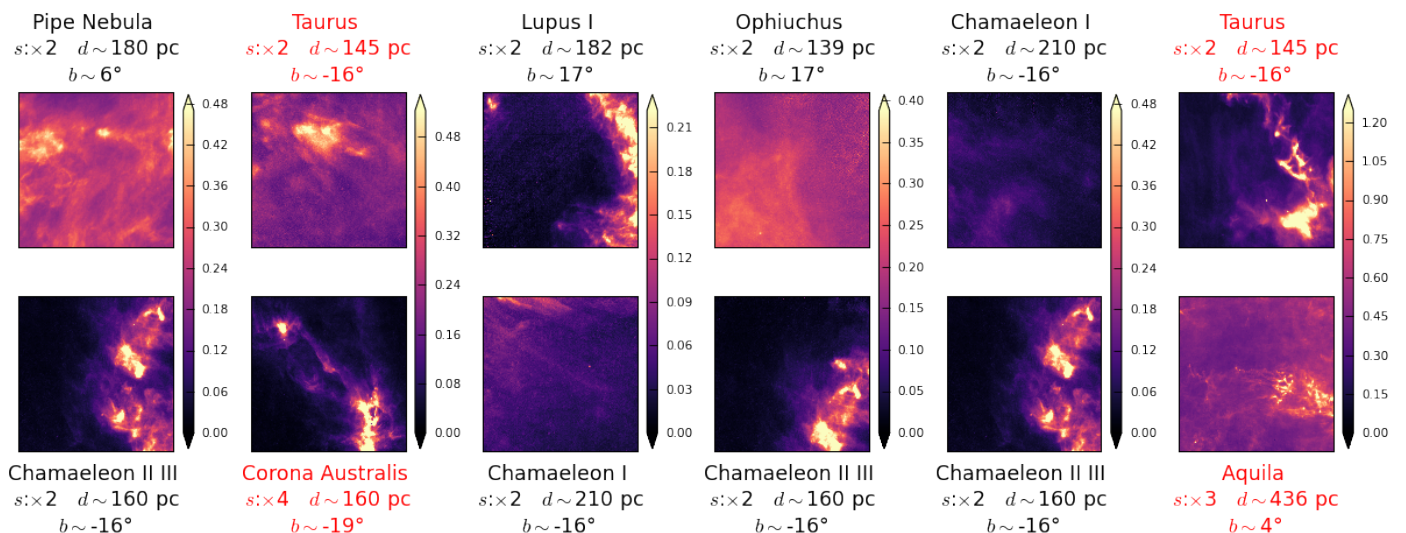


**Fig. 8.** Examples of Gaussian confusions. Six pairs of  $512 \times 512$  patches are chosen, whose locations on the scatter plot of Fig. 7 are given there by the red stars. The column density maps are shown in units of  $10^{20} \text{cm}^{-2}$ . For each patch, we report:  $s$  the sub-sampling factor from the original  $3''/\text{pix}$  map,  $d$  and  $b$  the approximated distance and Galactic latitude of the cloud. The pixel size (in mpc) of a patch is thus proportional to  $s \times d$ . If a pair has patches  $(i, j)$  with incompatible pixel sizes, that we define according to the following criterion  $\max\{\frac{s_i d_i}{s_j d_j}, \frac{s_j d_j}{s_i d_i}\} \geq 3/2$ , we color the labels in red.

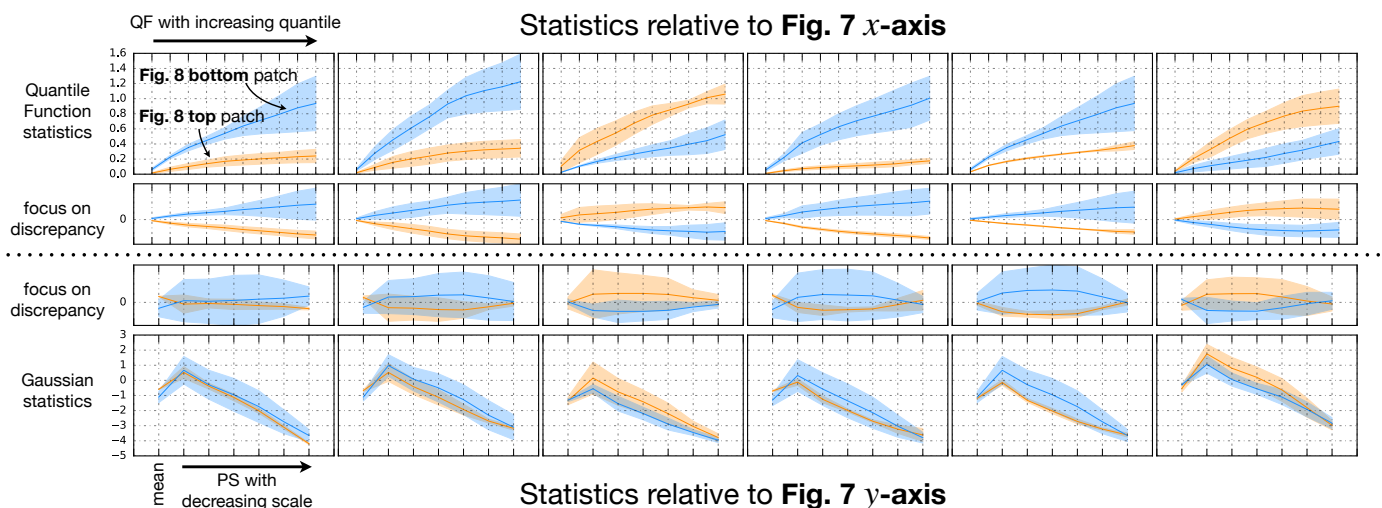


**Fig. 9.** Statistics for the examples of Gaussian confusions shown in Fig. 8. In each row, the orange filled line (resp. band) corresponds to the mean (resp. std) of the statistics computed over the four  $256 \times 256$  sub-patches of the top patch of each pair of Fig. 8, and the corresponding blue lines and areas refer to the bottom patch of the pair. The top row corresponds to the statistics used in the x-axis of the scatter plot of Fig. 7, *i.e.*, QF statistics, plotted with 10 increasing quantile values, while the bottom row corresponds to the y-axis, *i.e.*, Gaussian statistics, plotted starting with mean and followed by the binned PS with six decreasing scales. To better highlight the discrepancies between the two patches of a given pair, we report in second and third rows the offsets of the orange and blue filled lines with respect to their common mean.

deeper insights on the connection between regularity, approximation and sparsity, we recommend Pr. Mallat's lecture<sup>8</sup>. However, when dealing with datasets made of a wide diversity of irregular processes, such as everyday life textures like DTD, it is hard to identify a compression that does not lead, for some pairs, to poorer performances (c, f).

<sup>8</sup> <https://www.college-de-france.fr/fr/agenda/cours/representations-parcimonieuses/le-triangle-regularite-approximation-parcimonie>

## 5.2. Molecular clouds have log-Gaussian degeneracies

The ability of Gaussian one-point statistics to grasp efficiently one-point properties of observations from the logarithm of the column density maps, shown in Fig.10, suggests to shift towards log-Gaussian statistics, *i.e.*, mean and PS estimated on the logarithms of the maps. We thus investigate now whether we may point out some degeneracies of these statistics on observational data. However, if we confront this set with QF statistics, as we did previously for Gaussian statistics, we do not expect to lift significant log-Gaussian degeneracies. Instead, we suggest to search for such degeneracies using a higher order set: the RWST. To make sure that, on other datasets, the potential degen-

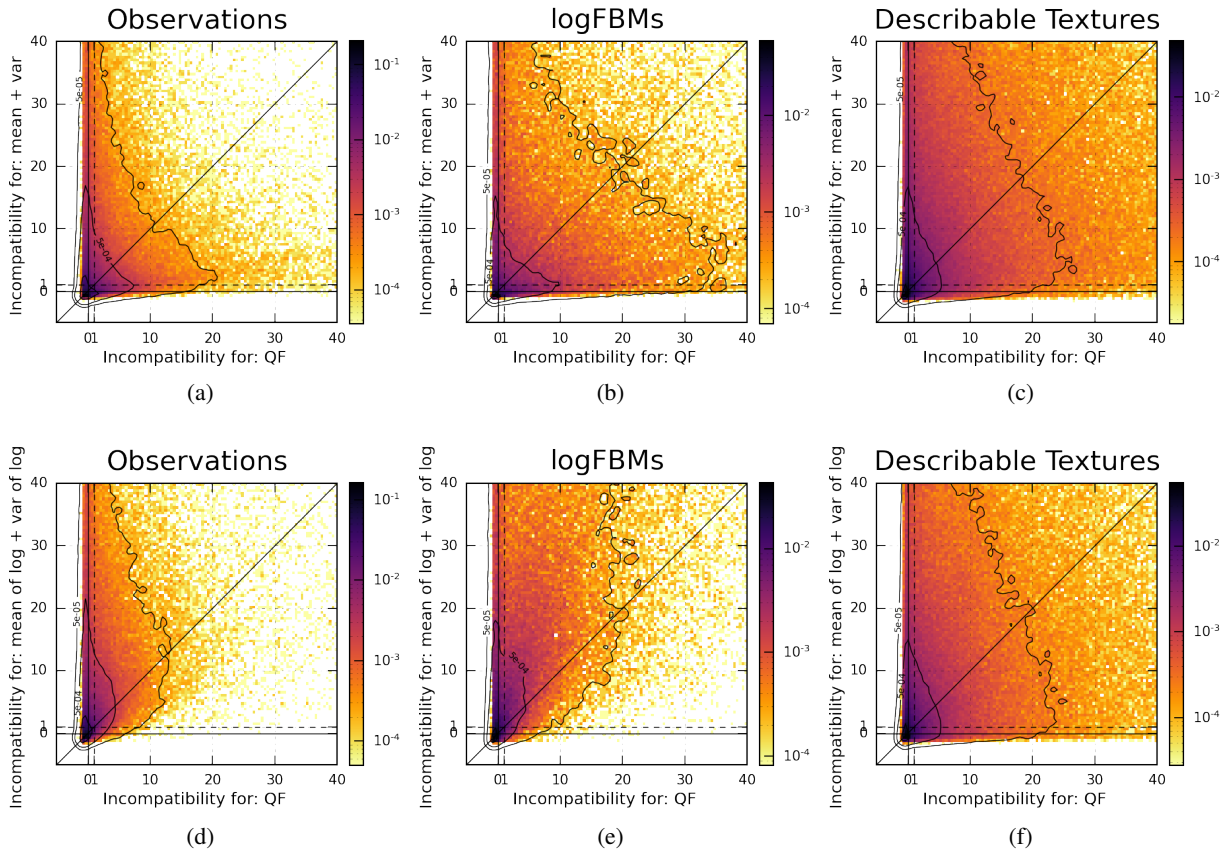


**Fig. 10.** Top row plots confront QF statistics to  $\{\phi_{\text{mean}}, \phi_{\text{var}}\}$ , while bottom row plots confront QF statistics to  $\{\phi_{\text{mean of log}}, \phi_{\text{var of log}}\}$ . These results evidence that taking the logarithm of the map enhances the discriminative power of the mean and variance statistics on both observation and logFBM data (left and middle columns) but not on DTD (right column).

eracies lifted by these higher order statistics could not be lifted by one-point statistics, we will confront the log-Gaussian set to the RWST one.

We show in Fig. 11 that log-Gaussian statistics have degeneracies on observational data lifted by RWST. We show six examples of degenerate pairs in Fig. 12 and the statistics of these patches in Fig. 13. In most of these pairs, the  $S_1^{Iso}$  coefficients heavily contribute to lift the log-Gaussian degeneracy. In the first and last pairs,  $\langle S_2^{Iso2} \rangle_{j_2-j_1}[\delta]$  and respectively  $\langle S_2^{Iso1} \rangle_{j_2-j_1}[\delta]$  are also very discriminative.

When applying the same analysis on logFBM data (Fig. 14.a), this finding however does not hold. The RWST diagnostic brings no additional information that was not already probed by log-Gaussian statistics. Indeed, as expected for such a dataset, log-Gaussian statistics are sufficient (Cover 1999). Finally, simulations yield yet another result (Fig. 14.b). Although this latter case leads to the same qualitative conclusions as observations, namely underlining the insufficiency of log-Gaussian statistics, it differs from it quantitatively. This supports the caveat of simulation-based inference according to which observations and simulations of such processes lie in sub-manifolds having different geometries, and motivates the observation-based approach of this paper.

### 5.3. Final set of statistics

In this paper, we choose to limit our study to the log-Gaussian + RWST set, which we call  $\phi_{\text{final}}$ , that seems well suited to describe this observational dataset. To ensure this suitability any

further, we could continue to study the degeneracies of  $\phi_{\text{final}}$  by confronting it with other sets of statistics. In any case, it is difficult to guarantee with certainty at any stage that we have not missed any remaining degeneracy of the resulting set that would be obtained by such a construction, even if each confrontation with a complementary set reinforces our confidence in its completeness.

Once a set of statistics has been fixed, however, it is also possible to use a complementary diagnostic to study it, which consists in checking the visual proximity of maps identified as close. If they are clearly visually different, this indicates complementary limitations of the set of statistics used. This is done with  $\phi_{\text{final}}$  in the following section, where we introduce a distance to evaluate a notion of proximity rather than compatibility between pairs of maps.

Finally, we want to emphasize that low-order statistics generally constitute a precious and easily-accessed source of information. They should not be underestimated, and attempting to tailor them to the type of data considered can be fruitful, as shown here when shifting from a Gaussian to a log-Gaussian description.

## 6. Comparing pairs and datasets

The previous section confronted multiple sets of statistics to assess their information content through their level of degeneracy. In this section, we fix the set of statistics:  $\phi = \phi_{\text{final}}$ , composed of 17 coefficients (7 log-Gaussian descriptors and 10 RWST statistics), and use it to define a distance between maps. We illustrate this distance by evidencing closest pairs of images in a dataset,

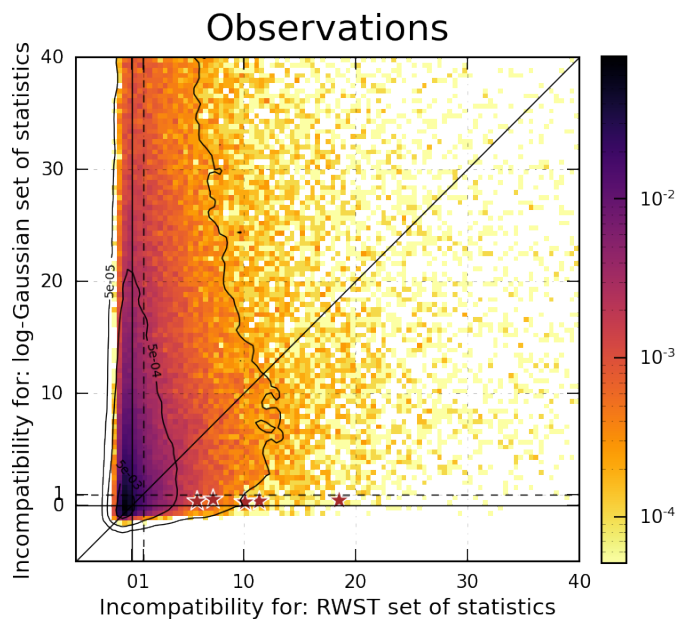


**Fig. 11.** Same as Fig. 7, but using the log-Gaussian and RWST sets of statistics on the observational dataset. To investigate the degeneracies of the log-Gaussian statistics, six pairs of patches are selected, corresponding to the six red stars on this plot.

as well as between different datasets such as observations and simulations.

### 6.1. Defining a morphological distance

Our objective is to define a distance between two patches based on  $\phi_{\text{final}}$ . One of our requirements is to enable a comparison between distance values for different pairs, so that these pairs can be ordered according to the morphological proximity of their patches. This requirement prevents us from using the statistical compatibility diagnostic introduced earlier. Indeed, since it is weighted by the local variance of each patch’s statistics, this can lead, for example, to some patches in a dataset being compatible with almost all the others simply because their spatial variance is very high. This could also encourage a simulation to approach an observation, following this criterion, by arbitrarily increasing its variance  $\text{Var} \phi(x_{SIM})$  without focusing on reducing the discrepancy of its average statistical properties  $\hat{\phi}(x_{SIM}) - \hat{\phi}(x_{OBS})$ . This property was purposely used to act as a penalization when confronting different sets of statistics in the previous section, but is no longer desired for pairs’ ordering, once  $\phi$  is fixed.

To build a distance that avoids this drawback, we choose instead to normalize it by the variability of the statistics evaluated over the entire observational dataset. We thus use the following distance:

$$d_{\mathcal{D}}^2(x_i, x_j) \equiv (\hat{\mu}_i - \hat{\mu}_j)^T (\text{diag } M_{\mathcal{D}})^{-1} (\hat{\mu}_i - \hat{\mu}_j), \quad (15)$$

which is normalized by the spanning of the estimated values  $\hat{\mu}_i$  of  $\phi_{\text{final}}$  over all maps of a given dataset  $\mathcal{D}$ :

$$M_{\mathcal{D}} \equiv \langle (\hat{\mu}_i - \langle \hat{\mu}_j \rangle_j) (\hat{\mu}_i - \langle \hat{\mu}_j \rangle_j)^T \rangle, \quad (16)$$

where the brackets indicate an average over  $\mathcal{D}$ . Note, however, that it is difficult to interpret the value of  $d_{\mathcal{D}}^2$  in absolute terms. Indeed, the  $M_{\mathcal{D}}$  term does not describe a typical variance for a

given process, but describes the variety of morphologies encountered in the entire dataset, that can be wide, as for the MC data investigated here. Unlike statistical compatibility diagnostics, the  $d_{\mathcal{D}}^2$  distance is therefore modified by the addition or removal of maps in the  $\mathcal{D}$  dataset, and can be affected by the presence of outliers.

In the following, we work with different datasets. For instance, we aim at comparing the minimum distance between observations and simulations to the typical distance of the closest pairs of observations. To do so, we use in this paper a common metric  $M_{\text{obs}}$  computed on the observation dataset, as well as the associated  $d_{\text{obs}}^2$  distance.

### 6.2. Closest pairs

We use the  $d_{\text{obs}}^2$  distance to identify the closest pairs of patches that can be found between two datasets. To do so, we report in Fig. 15 the cumulative distributions of distances associated to pairs of observation patches (in gray), as well as to pairs made of one observation patch and one logFBM, DTD, and simulation patch (in red, purple, and blue, respectively). For each case, we pick up six of the typical closest pairs<sup>9</sup>, as well as six relatively distant pairs, that we show in Fig. 16. In dashed lines with the same colors, we also report the cumulative distributions of distances associated to pairs of patches from a common dataset (logFBM, DTD<sup>10</sup>, and simulation patches, respectively).

Closest (OBS, OBS) pairs and (OBS, logFBM) pairs are visually rather similar, while distant pairs look very different. This relative agreement between morphological proximity as probed by our statistical distance as well as by human vision is encouraging, because it should be satisfied by an ideal distance. However, it remains far from being an exhaustive diagnostic.

The closest (OBS, logFBM) pairs have a distance  $d_{\text{obs}}^2 \sim 2$ , which marks a high agreement. Indeed, only  $\sim 0.5\%$  of (OBS, OBS) or (logFBM, logFBM) pairs exhibit smaller distance values, and we have already mentioned that the closest 1% of (OBS, OBS) pairs are very similar by construction. Comparatively, simulations are more distant to observations: the closest pairs between observations and simulations have a distance  $d_{\text{obs}}^2 \sim 8$ , four times larger than the closest (OBS, logFBM) pairs, when already  $\sim 10\%$  of pairs of observations exhibit smaller distances (see Sec. 6.3 for more details on this interpretation). As expected, these closest (OBS, SIM) pairs are visually less similar than the closest (OBS, OBS) or (OBS, logFBM) pairs (left panels of Fig. 16), but are still not so different, for instance with respect to the more distant pairs, that can be seen in the right panels of Fig. 16.

The closest (OBS, logFBM) samples obtained here are very diffuse regions of MCs such as Corona Australis, Polaris Flare, and Ophiuchus. This is not surprising because for MCs, diffuse regions are closer to logFBM models than dense regions, whose PDFs are known to deviate from log-normality. However, these diffuse regions are still supposed to exhibit coherent structures that should induce deviations from logFBM models. Here, such deviations are found to be small. We note, however, that this

<sup>9</sup> We do not investigate the  $\sim 1\%$  closest pairs of observations, since the comparison between observations is slightly biased with respect to the other ones. The reason is that, in that case only, we have pairs made of non independent patches, such as neighboring patches in the sky or two slightly different scaled versions of the same region. This corresponds to approximately 1% of the pairs, that we therefore exclude.

<sup>10</sup> Note that the  $\sim 10$  closest pairs of DTD images, located at  $d_{\text{obs}}^2 \lesssim 1$  are artifacts in this dataset corresponding in practice to almost identical images.

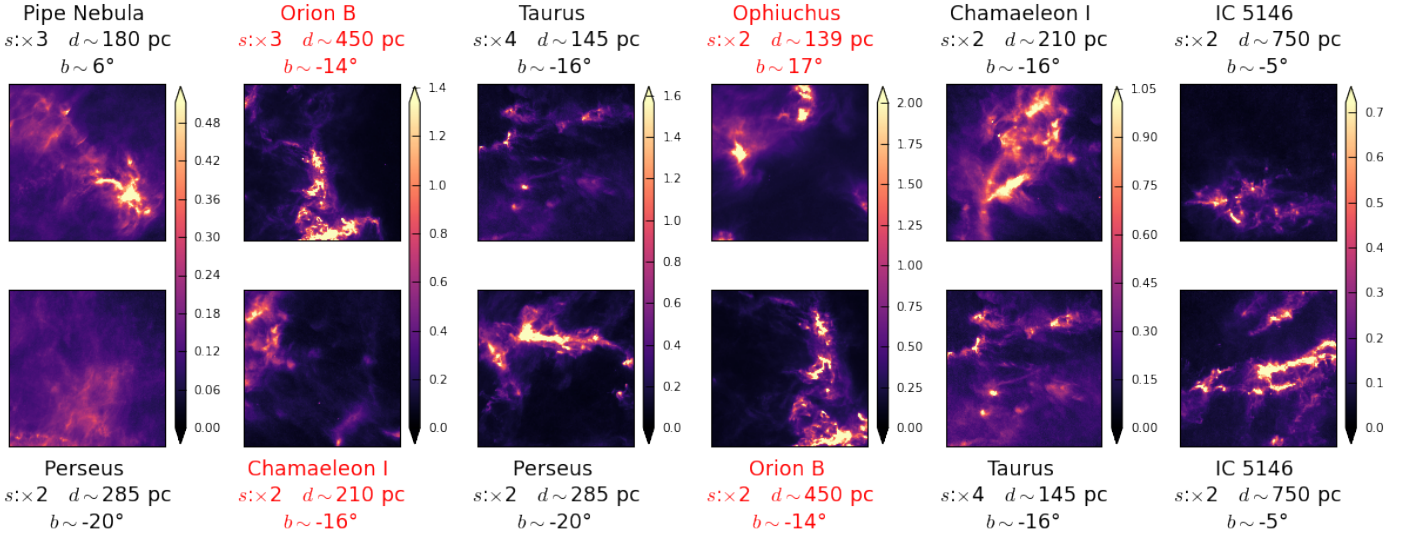


**Fig. 12.** Examples of log-Gaussian degeneracies. Six pairs of  $512 \times 512$  patches are chosen, whose locations on the scatter plot of Fig. 11 are given there by the red stars. The column density maps are shown in units of  $10^{20} \text{cm}^{-2}$ . For each patch, we report:  $s$  the sub-sampling factor from the original  $3''/\text{pix}$  map,  $d$  and  $b$  the approximated distance and Galactic latitude of the cloud. If a pair has patches  $(i, j)$  with incompatible pixel sizes according to the following criterion  $\max\{\frac{s_i d_i}{s_j d_j}, \frac{s_j d_j}{s_i d_i}\} \geq 3/2$ , we color the labels in red.

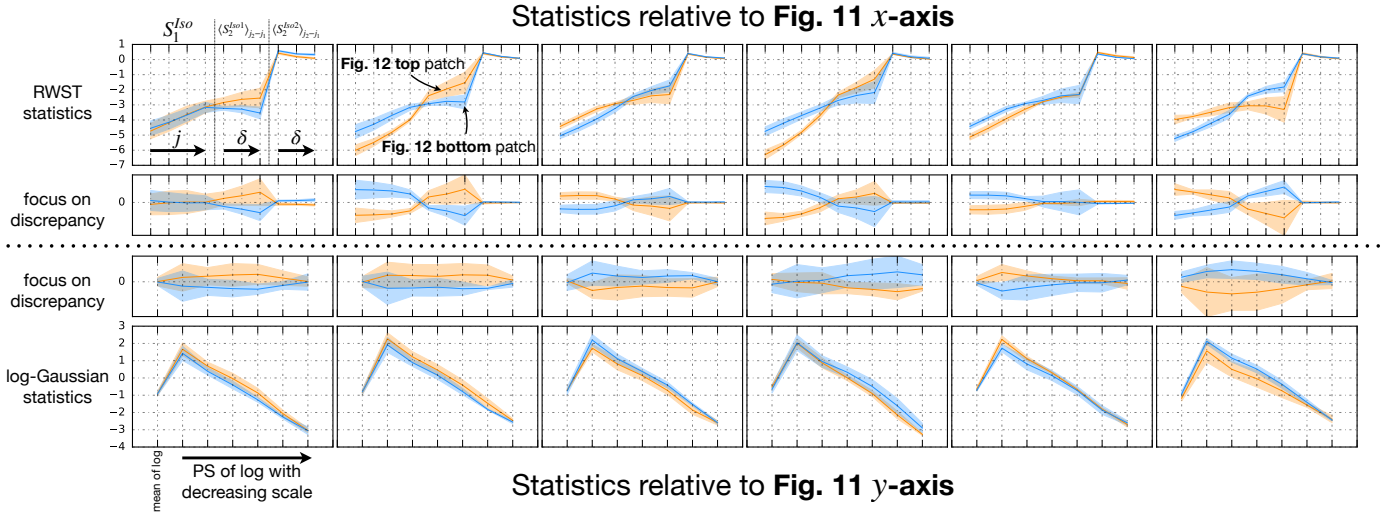


**Fig. 13.** Statistics for the examples of log-Gaussian confusions shown in Fig. 12. In each row, the orange filled line (resp. band) corresponds to the mean (resp. std) of the statistics computed over the four  $256 \times 256$  sub-patches of the top patch of each pair of Fig. 12, and the corresponding blue lines and areas refer to the bottom patch of the pair. The top row corresponds to the RWST, starting with  $S_1^{Iso}[j]$  coefficients with four increasing scales  $j$ , then  $\langle S_2^{Iso1} \rangle_{j_2-j_1}[\delta]$  coefficients with three increasing scale ratios  $\delta$  and finally  $\langle S_2^{Iso2} \rangle_{j_2-j_1}[\delta]$  coefficients with the same three scale ratios. The bottom row represents in the following order: mean of log followed by PS of log with 6 decreasing scales. The second and third rows show the offsets of these statistics with respect to the mean of the two.

proximity only means that certain diffuse regions are close to logFBM processes relative to the total variability of the observational dataset, and not necessarily that they are well described by such models, or could not be distinguished by the previous compatibility diagnostic. Moreover, this proximity to logFBM models is also partly due to contamination by the Cosmic Infrared Background (CIB), that has non negligible power at such low levels of column density, and is expected to Gaussianize the data, including their RWST statistics (Auclair et al. 2024). Incidentally, we remind that the observational dataset has some artifacts that make it deviate from an "ideal" MC column density

dataset, even if we try to limit as much as possible their effects (noise, finite resolution), as discussed in Sec. 4.

On the contrary, the observations that are closest to the simulations of dense MCs correspond, unsurprisingly, to dense regions of MCs such as Ophiuchus, Aquila, and Serpens. Note that Ophiuchus exhibits patches that are close to these dense simulations, but also at least one patch that is close to a logFBM model, underlining the spatial variability of molecular cloud morphologies. This illustrates the difficulty to treat a MC as a single entity, and emphasizes the relevance of our local approach.

The comparison between observations and DTD shows the limitations of our distance diagnostic. Indeed, the closest (OBS,

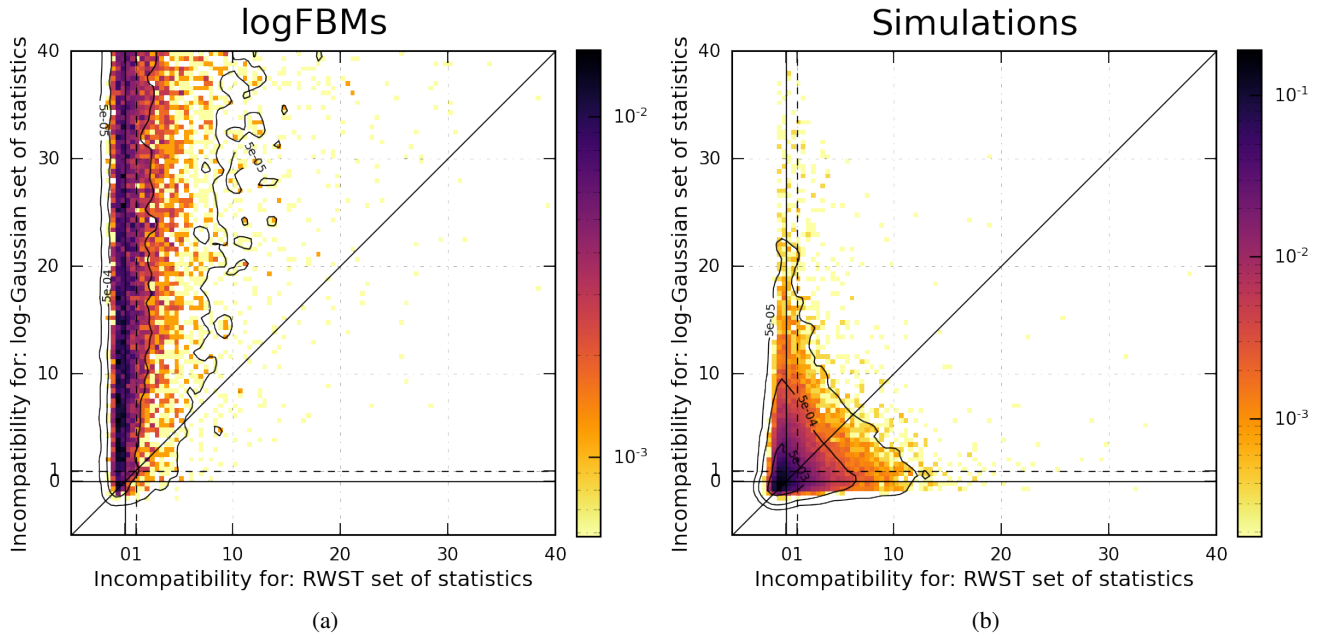


**Fig. 14.** log-Gaussian statistics have degeneracies lifted by RWST for simulations in (b), but not for logFBM processes in a). This is expected because log-Gaussian statistics are sufficient for families made of logFBM processes (Cover 1999).

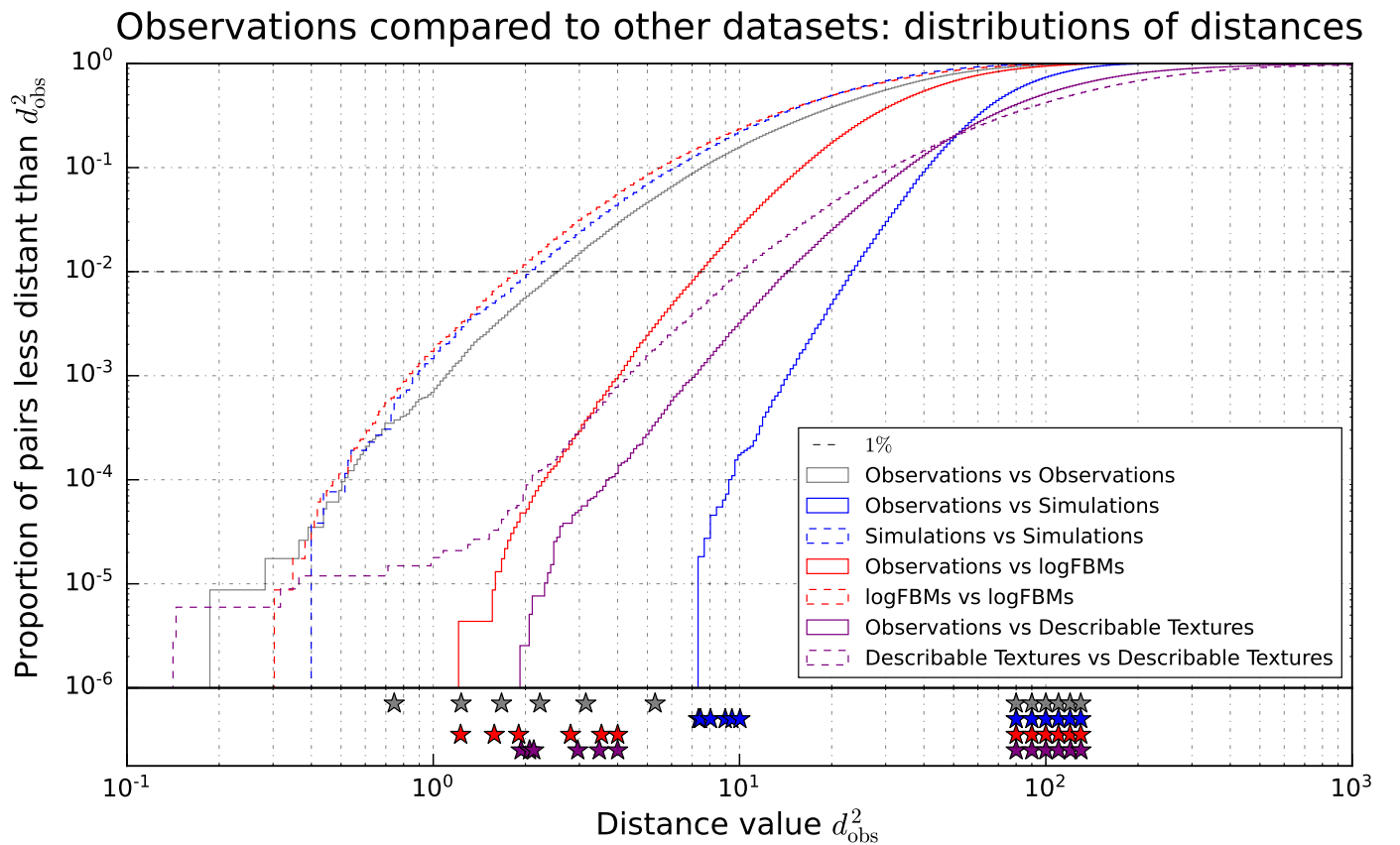


**Fig. 15.** Cumulative distributions of  $d_{\text{obs}}^2$  distances between pairs extracted from multiple datasets. The different curves correspond to different choices of datasets from which the two patches of a given pair are extracted. This distance is based on  $\phi_{\text{final}}$ , a set of 17 coefficients (7 log-Gaussian descriptors and 10 RWST statistics). The same metric  $M_{\text{obs}}$  is used for all distances and is defined based on the observational dataset. The stars in the bottom sub-panel correspond to "close" and "distant" pairs shown in Fig. 16. An horizontal line at the value 1% is drawn to represent the proportion of pairs of observations that are neighboring patches in the sky. For these pairs, the distance is underestimated and thus the gray curve below this line is not meaningful. Same applies for pairs of simulations (blue dashed curve).

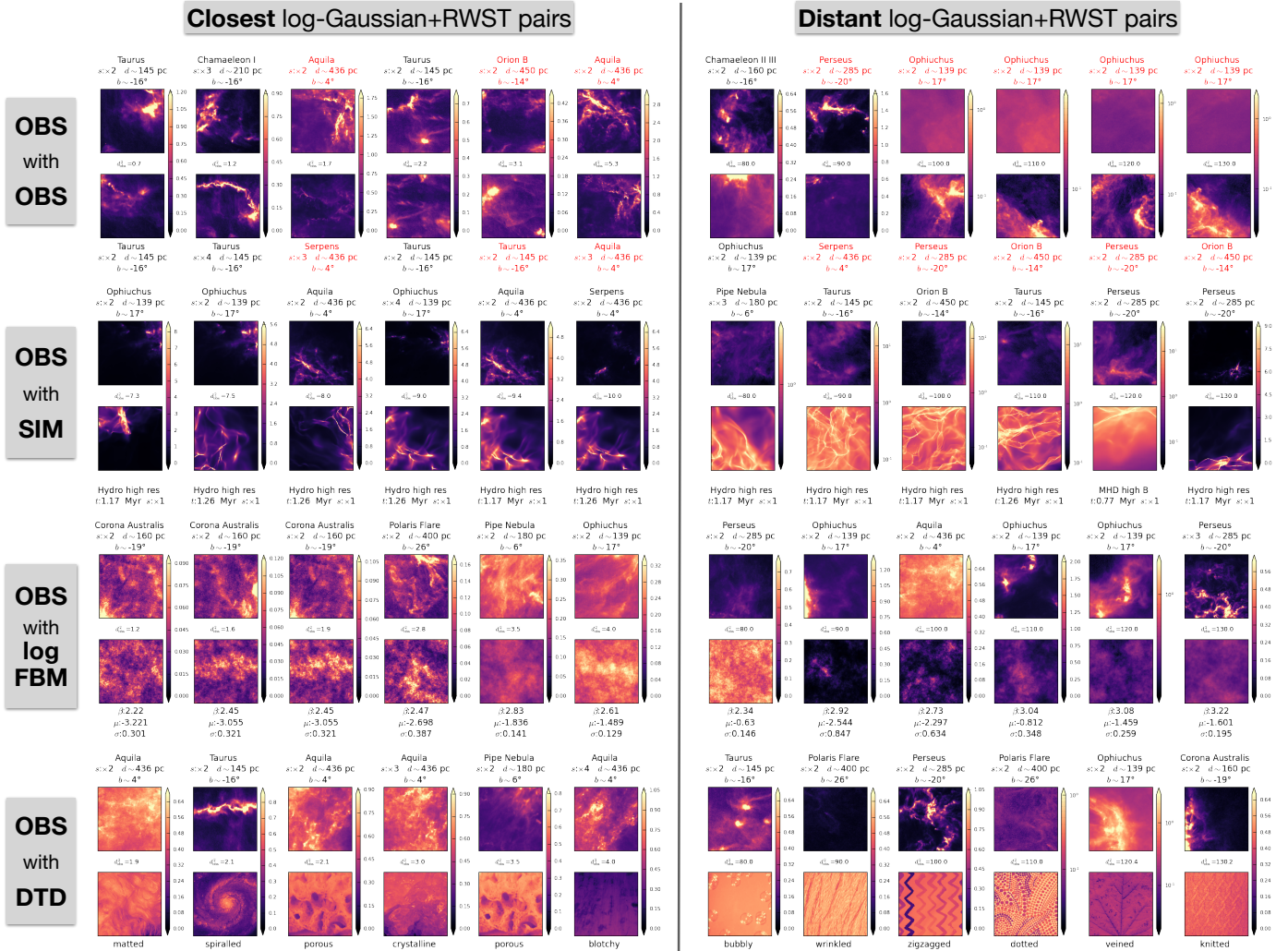


**Fig. 16.** Closest (left) and more distant (right) pairs extracted from distributions of distances reported in Fig. 15. We see that the closest (OBS, SIM) pairs are much more distant ( $d_{\text{obs}}^2 \sim 7$ ) than the closests (OBS, OBS) pairs ( $d_{\text{obs}}^2 \sim .7$ ). See Sec. 6.3 for more detailed interpretation on these results. Some logFBM models end up quite close to the most diffuse regions observed: Polaris Flare and Corona Australis. Such regions are highly contaminated by CIB emission. Many (OBS, DTD) pairs are found to be close whereas the textures look very different. This shows that the set of summary statistics developed in this paper is tuned for ISM observations but is far from being sufficient for any kind of data. This also illustrates that MCs have much more regularity in terms of morphology than DTD textures.

DTD) pairs are found at a distance  $d_{\text{obs}}^2 \sim 2$  that is the typical distance between close (OBS, OBS) pairs or close (OBS, logFBM) pairs, although they are visually very different. This illustrates that, for a diagnostic based on a low-dimensional set of statistics, it is difficult to probe a distance over a family of processes that has such a wide variety of textures as DTD. On the contrary, because the simulations that are closest to observations are more distant ( $d_{\text{obs}}^2 \sim 8$ ), this suggests that the set of simulations does not intersect the set of observations and that  $\phi_{\text{final}}$  is able to pinpoint this discrepancy, as discussed in the following subsection.

Finally, it is quite impressive to see that we can build a distance diagnostic from a representation of dimension 17 only that still manages to identify morphological similarity between maps quite satisfactorily. This illustrates the possibility of constructing a highly informative but low-dimensional description tailored to a family of processes from an ensemble of compressed sets of usual statistics. It should be stressed, however, that this study remains partial, notably because it is based mainly on the obser-

vation of a few close pairs in our dataset. Yet, the confrontation diagnostics studied in Sec. 5 showed that degenerate counterexamples remain largely in the minority. In addition, we lack solid baselines since it is inherently difficult to quantify visual impressions of morphological proximity, although some work has been done in this direction (Peek & White 2021).

### 6.3. Interpreting the minimal distance between observations and simulations

A last question we tackle is whether the relatively high value of the minimal distance  $d_{\text{obs}}^2$  that we get between observations and simulations indeed indicates distinct statistical properties of these two sets. More precisely, we question whether the set of observations' moments  $\{\bar{\mu}_i\}_{i \in \text{OBS}}$  overlaps that of simulations  $\{\bar{\mu}_j\}_{j \in \text{SIM}}$ , where  $\bar{\mu}_i \equiv \mathbb{E}[\phi_{\text{final}}(x_i)]$  stands for the expected value over a given process  $i$ . In practice, we aim at retrieving the min-

imal distance

$$\bar{d}_{ij}^2 \equiv (\bar{\mu}_i - \bar{\mu}_j)^T (\text{diag } M_{\text{obs}})^{-1} (\bar{\mu}_i - \bar{\mu}_j) \quad (17)$$

between  $\bar{\mu}_i$  and  $\bar{\mu}_j$  over (OBS, SIM) pairs  $(i, j)$ . However, the distance  $d_{\text{obs}}^2$  introduced previously is a statistical estimator, so that in general

$$d_{ij}^2 \neq \bar{d}_{ij}^2,$$

and in particular:  $\mathbb{E}[d_{ij}^2] > \bar{d}_{ij}^2$ . Indeed, the variance of the  $\hat{\mu}_i$  estimator biases  $d_{ij}^2$  with respect to  $\bar{d}_{ij}^2$ :

$$\mathbb{E}[d_{ij}^2] \equiv \bar{d}_{ij}^2 + b_{ij}. \quad (18)$$

This non-negative bias, which boils down to:

$$b_{ij} = \text{tr}[\text{cov}[(\text{diag } M_{\text{obs}})^{-1/2}(\hat{\mu}_i - \hat{\mu}_j)]], \quad (19)$$

prevents us from interpreting directly the value of  $d_{ij}^2$  as  $\bar{d}_{ij}^2$ . Furthermore, its value increases with the amplitude of the fluctuations of  $\hat{\mu}_i - \hat{\mu}_j$ , and can thus change depending on the pair  $(i, j)$  considered. This dependency on the pair also prevents us, without further check, from actually comparing  $d^2$  between different pairs based on the estimations  $d^2$ .

To probe and interpret the minimal distance between observations and simulations, we propose the following strategy:

- find an observation  $i$  and a simulation  $j$  that minimize the biased estimation  $d_{ij}^2$ . Such pairs are already reported in Fig.16 and are good candidates to minimize  $\bar{d}_{ij}^2$ . The goal then becomes to compare  $\bar{d}_{ij}^2$  to the minimal value  $\bar{d}_{i'j'}$ , for  $i'$  another observation, independent from  $i$ . But  $\bar{d}^2$  is unknown. Instead:
- find an observation  $i'$ , that minimizes the biased distance  $d_{i'j'}$ , while checking it does not overlap  $i$  in the sky to assume them independent.
- Since  $\bar{d}_{ij}^2 - \bar{d}_{i'j'}^2 = \mathbb{E}[d_{ij}^2] - \mathbb{E}[d_{i'j'}^2] + b_{i'j'} - b_{ij}$ , the discrepancy between  $\bar{d}_{ij}^2 - \bar{d}_{i'j'}^2$  can be estimated based on the measured discrepancy  $d_{ij}^2 - d_{i'j'}^2$  up to the unknown bias shift  $b_{i'j'} - b_{ij}$ .
- If, in addition the observation patch  $x_{i'}$  is such that spatial fluctuations of  $\phi_{\text{final}}$  over its sub-patches are at least of the order of those estimated from the sub-patches of the simulation patch  $x_j$ , then based on Eq. 19, we have  $b_{i'j'} \gtrsim b_{ij}$ . This allows then to use  $d_{ij}^2 - d_{i'j'}^2$  as an estimated lower bound for  $\bar{d}_{ij}^2 - \bar{d}_{i'j'}^2$ .

We report in Fig. 17 such independent<sup>11</sup> pairs  $(i, i')$ . In the first row, we fix  $i$  associated to the patch of Ophiuchus  $x_i$  that is the closest observation to simulations ( $d_{ij}^2 = 7$ , Fig.16). For that choice of patch, the reported distances  $d_{i'j'}^2$  of neighboring observations  $i'$  are rather similar to  $d_{ij}^2$ . However, in the second row, where  $i$  is associated to the patch of Aquila that is the second closest observation to simulations (as shown in Fig.16), we see other observations  $i'$ , such as Serpens or Orion B, that are closer than the closest simulation:  $d_{i'j'}^2 = 3 < d_{ij}^2 = 8$ . We checked that the fluctuations of  $i'$  are comparable to the one of  $j$  so that  $b_{i'j'} \gtrsim b_{ij}$ . This implies then  $\bar{d}_{ij}^2 - \bar{d}_{i'j'}^2 \gtrsim 5$  while  $\bar{d}_{i'j'}^2 \leq d_{i'j'}^2 = 3$ . Hence,  $\bar{d}_{ij}^2/\bar{d}_{i'j'}^2 \gtrsim 8/3$ . This second case shows that one of the closest

observation/simulation pair is definitely further apart than this specific observation is with other observations, at least according to  $\phi_{\text{final}}$ . This example also supports that the potential bias on the  $d_{\text{obs}}^2$  estimators remains moderate for the study of (OBS, SIM) pairs ( $\bar{d}_{ij}^2 \gtrsim 5$  and  $d_{ij}^2 = 8$  implies  $b_{ij} \gtrsim 3$ ).

We conclude that the minimum (OBS, SIM) distance value, obtained on all possible pairs between those datasets, evidences a meaningful but moderated distinction between these datasets. Note that the  $\phi_{\text{final}}$  statistics set may still have some degeneracies, particularly for the (OBS, SIM) comparison, and that accounting for these should likely deepen this gap. We however believe that current analysis illustrates the usefulness of such a distance, and leave a more detailed study for future work.

## 7. Conclusions

In this paper, we aim at studying the diversity of morphologies of observed molecular clouds. To do so we construct a set of  $\sim 500$  patches of size  $512 \times 512$  pixels, extracted at different resolutions from column density maps of 14 nearby clouds derived from the HGBS dust emission observations. We compute several sets of statistics (mean, variance, quantile function, power spectrum and scattering transform) from these maps, and we compare their informative power. To do so, we introduce a new methodology (Fig. 6) that allows to confront, without any supervision, two sets of summary statistics on their respective abilities to detect statistical incompatibility between pairs of processes in a given dataset.

Applying this methodology to this set of observations, we find that Gaussian statistics have degeneracies for the observational dataset, some of which can be lifted by one-point statistics (Fig. 7). We then show that even if log-Gaussian statistics are much less degenerate, a compressed set of scattering statistics still succeeds to demonstrate further degeneracies (Fig. 11). This confirms that the diversity of morphologies arising in these observed clouds cannot be sufficiently described by Gaussian nor log-Gaussian statistics. This means that using such descriptions, typically to compare numerical simulations with observational data, can lead to misleading projections: in addition to missing potential absolute discrepancies, observations with different properties can still be matched to the same simulation.

We apply the same diagnostic to simulations and to the set of logFBMs (Fig. 14), and find deviations from observations' geometry. In particular, the outcome of this diagnostic strikingly supports the sufficiency of log-Gaussian statistics to discriminate between logFBM patches. Regarding observations and simulations, there remain deviations between their respective geometries, even though great care has been taken in this work to design robust and low dimensional sets of summary statistics. This supports the difficulty of transferring simulation-based priors<sup>12</sup> to observations, especially high-order information content, and also buttresses the supervision-detached approach developed in this paper, along with the choice to work with compressed and robust summary statistics.

From these results, we introduce a morphological distance  $d_{\text{obs}}^2$  based on a set of summary statistics  $\phi_{\text{final}}$  composed of 7 log-Gaussian and 10 RWST coefficients. The similarity probed by this distance is in agreement with visual impression when comparing observations with themselves, with logFBMs and with simulations (Fig. 16). It remains however insufficient to operate on datasets made of a wider diversity of textures such as

<sup>11</sup> Indeed, only one of these pairs is made of patches retrieved from the same MC (Ophiuchus), but these patches do not overlap.

<sup>12</sup> Such as the outcome of a Fisher analysis, or a trained neural network.



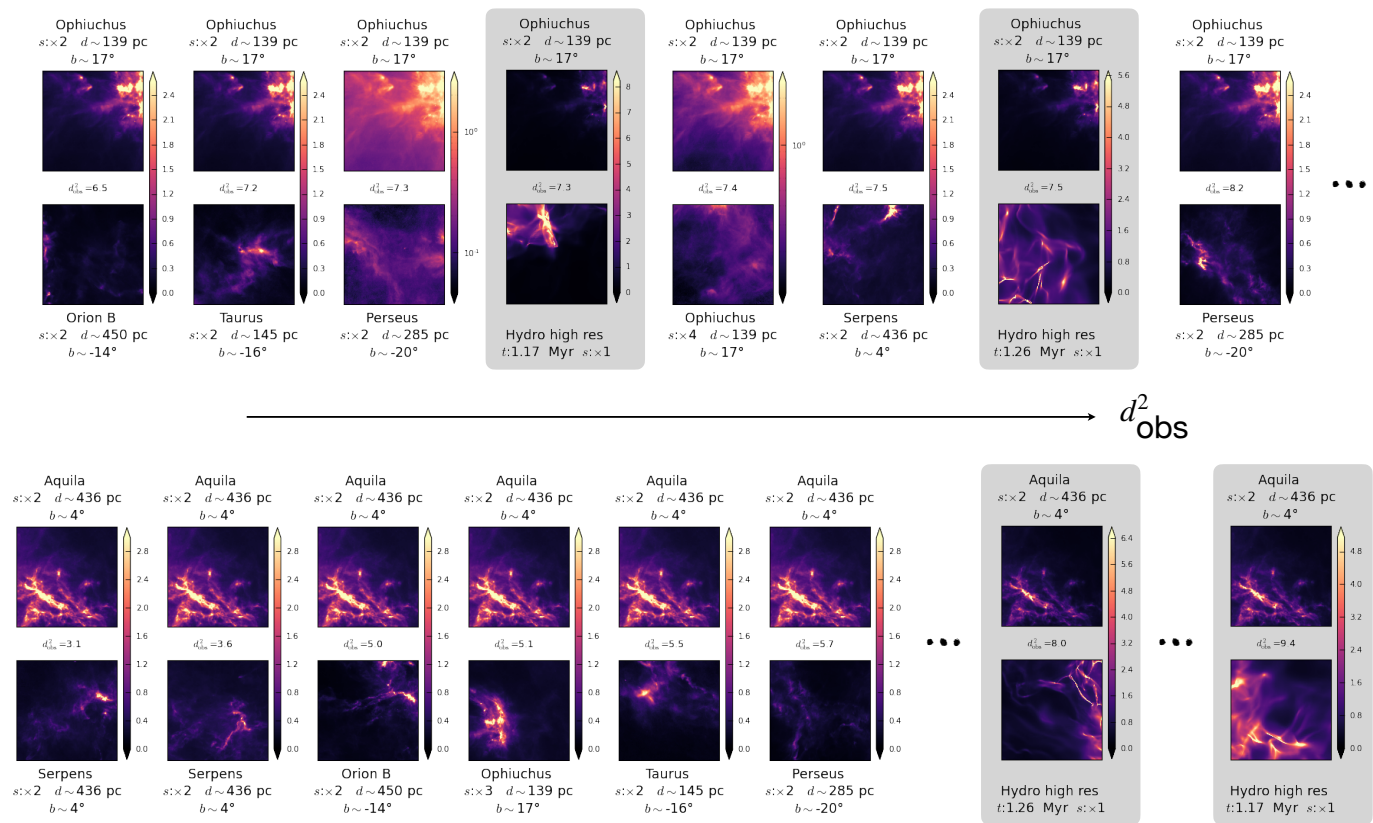


**Fig. 17.** Comparing closest (OBS, SIM) pairs ( $i, j$ ) (gray boxes) to neighboring (OBS, OBS) pairs ( $i, i'$ ). Top row focuses on the closest observation to simulations, that is a patch of Ophiuchus, while bottom row focuses on the second closest patch, that is in Aquila cloud. In the latter case, neighboring (but independent) observations of Aquila are closer than the closest simulations. The color-bars can change from a pair to another.

DTD.

This work opens multiple perspectives:

- the methodology we developed to confront summary statistics requires very few assumptions: it can operate in an unsupervised and very low data regime. Hence such methodology can easily be assimilated by the ISM community and applied on a wider set of statistics and physical tracers of data (velocities, polarization, temperature).
- The low dimensional and analytical morphological embedding  $\phi_{\text{final}}$  developed here allows for a directly interpretable comparison, for instance between different observed clouds, between observations and simulations or statistical models, but it also paves the way for the use of more sophisticated unsupervised learning techniques.
- Leveraging saliency maps  $\nabla_{\text{pixels}} d_{\text{obs}}^2(x_i, x_j)$ , the distance  $d_{\text{obs}}^2$  can be used to highlight the main areas responsible for morphological discrepancies between two patches ( $x_i, x_j$ ), broadening the scope of the work initiated by Peek & Burkhart (2019) to the unsupervised world of observations.
- The confrontation methodology can be used to make a feature selection algorithm, in the spirit of the FRAME model developed by Zhu et al. (1998), but designed to optimize the comparison task of a non-parametric collection of processes  $\{p_i\}_i$ , instead of modeling a single process.

The following improvements could also be of great benefit:

- reduce the uncertainty in the compatibility diagnostic  $d_{\phi}^2$  due to the precision matrix estimation. A promising idea is to use

a maximum entropy model conditioned on the data on which to perform the precision estimation.

- Reduce the overall dependency of the distance  $d_{\mathcal{D}}^2$  on the dataset  $\mathcal{D}$ , and in particular on its outliers. This can be done by building a localized metric, based on local estimations of the geometry, restricting  $\mathcal{D}$  to  $\mathcal{D}_{\text{loc}}[i]$ , the neighbors of a given process  $i$ .

*Acknowledgements.* This research has made use of data from the *Herschel* Gould Belt survey (HGBS) project<sup>13</sup>. The HGBS is a *Herschel* Key Programme jointly carried out by SPIRE Specialist Astronomy Group 3 (SAG 3), scientists of several institutes in the PACS Consortium (CEA Saclay, INAF-IFSI Rome and INAF-Arcetri, KU Leuven, MPIA Heidelberg), and scientists of the *Herschel* Science Center (HSC).

This work reused datasets available on the Galactica simulations database<sup>14</sup>. This work reused the Describable Textures Dataset<sup>15</sup>.

## References

- Allys, E., Levrier, F., Zhang, S., et al. 2019, A&A, 629, A115, publisher: EDP Sciences
- André, P., Di Francesco, J., Ward-Thompson, D., et al. 2014, Protostars and Planets VI, 27
- André, P., Men'shchikov, A., Bontemps, S., et al. 2010, A&A, 518, L102
- Appel, S. M., Burkhart, B., Semenov, V. A., Federrath, C., & Rosen, A. L. 2022, The Astrophysical Journal, 927, 75
- Arzoumanian, D., André, P., Didelon, P., et al. 2011, Astronomy & Astrophysics, 529, L6
- <sup>13</sup> <http://gouldbelt-herschel.cea.fr>
- <sup>14</sup> <http://www.galactica-simulations.eu>
- <sup>15</sup> <https://www.robots.ox.ac.uk/~vgg/data/dtd/>

- Auclair, C., Allys, E., Boulanger, F., et al. 2024, *Astronomy & Astrophysics*, 681, A1
- Bruna, J. & Mallat, S. 2013, *IEEE transactions on pattern analysis and machine intelligence*, 35, 1872
- Brunt, C. M. & Heyer, M. H. 2002, *The Astrophysical Journal*, 566, 276
- Burkhart, B., Falceta-Gonçalves, D., Kowal, G., & Lazarian, A. 2009, *The Astrophysical Journal*, 693, 250
- Burkhart, B. & Lazarian, A. 2016, *The Astrophysical Journal*, 827, 26
- Cimpoi, M., Maji, S., Kokkinos, I., et al. 2014, in *Proceedings of the IEEE Conf. on Computer Vision and Pattern Recognition (CVPR)*
- Cover, T. M. 1999, *Elements of information theory* (John Wiley & Sons)
- Elmegreen, B. G. 2002, *The Astrophysical Journal*, 564, 773
- Falgarone, E., Hily-Blant, P., & Levrier, F. 2004, *Ap&SS*, 292, 89
- Federrath, C. & Klessen, R. S. 2013, *The Astrophysical Journal*, 763, 51
- Fromang, S., Hennebelle, P., & Teyssier, R. 2006, *A&A*, 457, 371
- Galli, P. A. B., Bertout, C., Teixeira, R., & Ducourant, C. 2013, *A&A*, 558, A77
- Goodman, A. A., Rosolowsky, E. W., Borkin, M. A., et al. 2009, *Nature*, 457, 63
- Heithausen, A. & Thaddeus, P. 1990, *ApJ*, 353, L49
- Hennebelle, P. & Chabrier, G. 2008, *The Astrophysical Journal*, 684, 395
- Heyer, M. H. & Brunt, C. M. 2004, *The Astrophysical Journal*, 615, L45
- Hotelling, H. 1931
- Kainulainen, J., Beuther, H., Henning, T., & Plume, R. 2009, *Astronomy & Astrophysics*, 508, L35
- Knude, J. & Hog, E. 1998, *A&A*, 338, 897
- Könyves, V., André, P., Men'shchikov, A., et al. 2015, *Astronomy & Astrophysics*, 584, A91, publisher: EDP Sciences
- Levrier, F., Falgarone, E., & Viallefond, F. 2006, *Astronomy & Astrophysics*, 456, 205
- Levrier, F., Neveu, J., Falgarone, E., et al. 2018, *Astronomy & Astrophysics*, 614, A124
- Mamajek, E. E. 2008, *Astronomische Nachrichten*, 329, 10
- McKee, C. F. & Ostriker, E. C. 2007, *ARA&A*, 45, 565
- Miville-Deschênes, M.-A., Lagache, G., Boulanger, F., & Puget, J.-L. 2007, *Astronomy & Astrophysics*, 469, 595
- Miville-Deschênes, M. A., Martin, P. G., Abergel, A., et al. 2010, *A&A*, 518, L104
- Ntormousi, E. & Hennebelle, P. 2019, *Astronomy & Astrophysics*, 625, A82
- Ortiz-León, G. N., Loinard, L., Dzib, S. A., et al. 2018, *ApJ*, 869, L33
- Ossenkopf-Okada, V., Csengeri, T., Schneider, N., Federrath, C., & Klessen, R. S. 2016, *Astronomy & Astrophysics*, 590, A104
- Palmeirim, P. a., André, P., Kirk, J., et al. 2013, *Astronomy & Astrophysics*, 550, A38
- Park, C. F., Allys, E., Villaescusa-Navarro, F., & Finkbeiner, D. 2023, *The Astrophysical Journal*, 946, 107
- Peek, J. & Burkhart, B. 2019, *The Astrophysical Journal Letters*, 882, L12
- Peek, J. & White, R. 2021, *Bulletin of the AAS*, 53, <https://baas.aas.org/pub/2021n6i301p06>
- Pilbratt, G. L., Riedinger, J. R., Passvogel, T., et al. 2010, *A&A*, 518, L1
- Planck Collaboration. 2020, *A&A*, 641, A12
- Pouteau, Y., Motte, F., Nony, T., et al. 2023, *A&A*, 674, A76
- Regaldo-Saint Blancard, B., Levrier, F., Allys, E., Bellomi, E., & Boulanger, F. 2020, *Astronomy & Astrophysics*, 642, A217
- Remazeilles, M., Delabrouille, J., & Cardoso, J.-F. 2011, *MNRAS*, 418, 467
- Robitaille, J.-F., Motte, F., Schneider, N., Elia, D., & Bontemps, S. 2019, *Astronomy & Astrophysics*, 628, A33
- Saydjari, A. K., Portillo, S. K., Slepian, Z., et al. 2021, *The Astrophysical Journal*, 910, 122
- Schekochihin, A. A. 2022, *Journal of Plasma Physics*, 88, 155880501
- Schlaflly, E. F., Green, G., Finkbeiner, D. P., et al. 2014, *ApJ*, 786, 29
- Schneider, N., André, P., Könyves, V., et al. 2013, *ApJ*, 766, L17
- Schneider, N., Ossenkopf-Okada, V., Clarke, S., et al. 2022, *Astronomy & Astrophysics*, 666, A165
- Srivastava, M. S. & Du, M. 2008, *Journal of Multivariate Analysis*, 99, 386
- Teyssier, R. 2002, *A&A*, 385, 337
- Vázquez-Semadeni, E., Ballesteros-Paredes, J., & Rodríguez, L. F. 1997, *The Astrophysical Journal*, 474, 292
- Yan, Q.-Z., Zhang, B., Xu, Y., et al. 2019, *A&A*, 624, A6
- Zavagno, A., Dupé, F.-X., Bensaid, S., et al. 2023, *Astronomy & Astrophysics*, 669, A120
- Zhu, S. C., Wu, Y., & Mumford, D. 1998, *International Journal of Computer Vision*, 27, 107
- Zucker, C., Speagle, J. S., Schlaflly, E. F., et al. 2020, *A&A*, 633, A51

## Appendix A: Other datasets

### Appendix A.1: Numerical simulations

The set of numerical simulations used in this paper as an example of state-of-the-art attempts to reproduce the physics of the ISM *in silico* is taken from the ORION project of the Galactica database<sup>16</sup>. Using the adaptive mesh refinement (AMR) code RAMSES (Teyssier 2002; Fromang et al. 2006), the data simulates the collapse of a dense molecular cloud under self-gravity, including decaying MHD turbulence but without stellar feedback. The focus of these simulations is to study the early stages of the star formation process in a molecular cloud ( $10^5 M_{\odot}$  in a 66 pc cubic box), and so fits in well with the HGBS observational data used in this paper.

Three classes of simulations are considered, one without magnetic field ("Hydro high res"), one with a typical magnetic field of order  $5 - 10 \mu\text{G}$  ("MHD"), and one with a higher value of the magnetic field of order  $10 - 25 \mu\text{G}$  ("MHD high B"). With the adaptive mesh refinement scheme, the spatial resolution of the models can reach down to 1 mpc ( $\sim 200$  au), and even 100 au for the "Hydro high res" model. For more details about these simulations, we refer the reader to Ntormousi & Hennebelle (2019).

For each of these models, we take two snapshots, integrate along the three axes, and crop the resulting column density images to keep the central  $33 \text{ pc} \times 33 \text{ pc}$  field, on a regular  $4096 \times 4096$  grid. Examples of such images are shown in Fig. A.1. As we did for observations, we cut these panels into  $512 \times 512$  patches, keeping only the ones where the effective resolution is fine enough, to avoid artifacts due to the AMR scheme affecting our morphological analysis. The pixels in the resulting patches have sizes 8 mpc. This is in accordance with the typical spatial sampling found in our observational dataset. Indeed, this corresponds to the finest pixels ( $6''$ ) of intermediate-distance clouds  $d \sim 300 \text{ pc}$ , but also to the closest clouds  $d \sim 150 \text{ pc}$  sampled at  $12''$ .

### Appendix A.2: logFBM models

To perform our analysis of observational data, we also consider purely synthetic, parametric models of column density maps, derived from exponentiations of fractional Brownian motions (fBm). Such fields have been previously studied by the ISM community (Elmegreen 2002; Brunt & Heyer 2002; Miville-Deschênes et al. 2007; Levrier et al. 2018). It is indeed a convenient class of models that allows to simultaneously reproduce exactly the log-normal one-point properties (encountered in quiescent regions) and power-law power spectra to a good approximation. An example is given in Fig. 1.

In this paper, we consider the following model:

$$X \equiv e^{\sigma F_{\beta} \star Z + \mu}, \quad \text{with } Z \sim \mathcal{N}(\mathbf{0}, I), \quad (\text{A.1})$$

parametrized by  $\mu$ ,  $\sigma$  and  $\beta$ , corresponding respectively to the mean, standard deviation and spectral index of the fBm. The latter is generated by sampling a  $512 \times 512$  Gaussian white noise map  $Z$ , which is then filtered with  $F_{\beta}$ , that is defined in Fourier space as:

$$\tilde{F}_{\beta}(\mathbf{k}) \equiv \begin{cases} \propto k^{-\beta/2} & \text{if } \mathbf{k} \neq \mathbf{0}, \\ 1 & \text{if } \mathbf{k} = \mathbf{0}, \end{cases} \quad (\text{A.2})$$

such that  $\sigma F_{\beta} \star Z + \mu$  is a real valued Gaussian process with mean  $\mu$ , variance  $\sigma^2$  and  $\beta$ -decaying power spectrum power-law.

<sup>16</sup> [http://www.galactica-simulations.eu/db/STAR\\_FORM/ORION/](http://www.galactica-simulations.eu/db/STAR_FORM/ORION/)

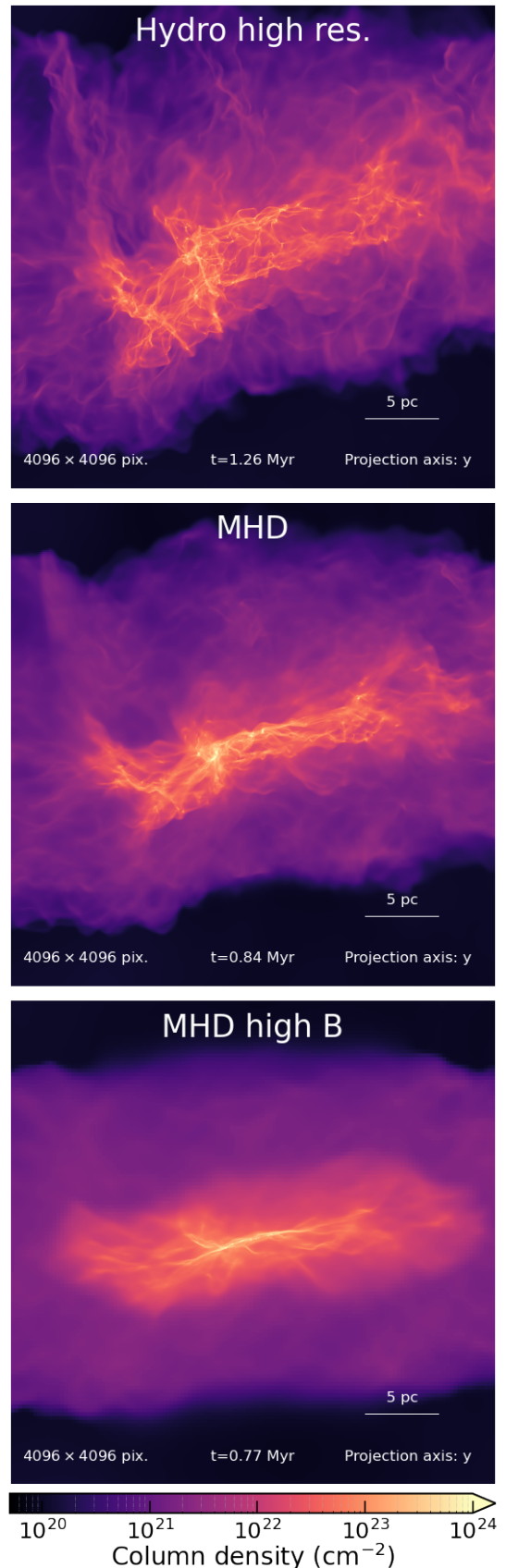


**Fig. A.1.** Overview of the simulations. One snapshot is shown for each model ("Hydro high res", "MHD", and "MHD high B"), and the maps show the central  $33 \text{ pc} \times 33 \text{ pc}$  field for gas column density integrated along the y axis.

The parameters  $(\mu, \sigma, \beta)$  are fitted from the observations. More precisely, for each  $512 \times 512$  column density patch that has no negative pixel (that is about 87% of the 550 observational patches), we estimate the mean  $\mu$ , variance  $\sigma^2$  and spectral index  $\beta$  on the logarithm of the column density patch, expressed in  $10^{22} \text{ cm}^{-2}$  units. This procedure leads to a distribution of  $\sim 480$  estimated parameters triplets  $(\mu, \sigma, \beta)$  that is reported in Fig. A.2. For each triplet, we then sample one  $512 \times 512$  logFBM patch. Contrary to the other patches considered in this paper (observations, simulations, everyday textures), these samples have periodic boundary conditions, by construction. However, their  $256 \times 256$  sub-patches, that are the only ones on which the various summary statistics are applied, do not, just as the rest of the data.

We dub these synthetic maps logFBM models, to recall that the statistics of their logarithms are those of the Gaussian, fBM random fields. In the literature, emission maps are often produced by integrating a 3D generated field. In this paper, for simplicity and computational efficiency, we directly generate 2D fields. Even though integrated 3D fields could be expected to better model MCs' column density maps, they do not differ much in morphology from 2D models and both are far from reproducing MCs' morphology. Thus, the 2D logFBM models used here are suited to the scope of this paper.

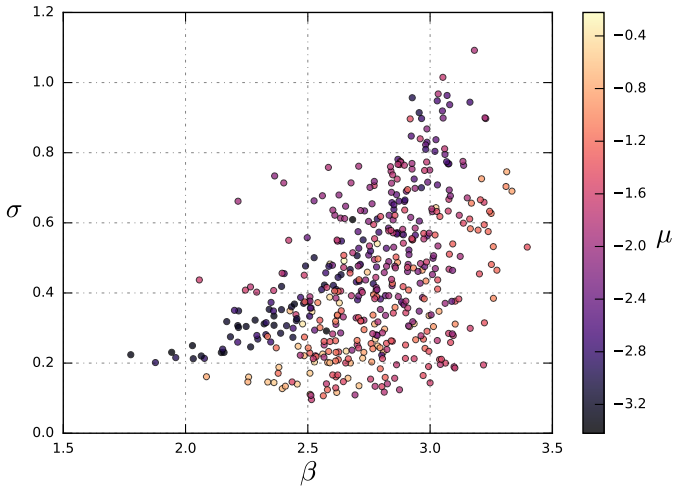


**Fig. A.2.** log-Gaussian parameters fitted on the observations used to sample logFBM data.

### Appendix A.3: Describable Textures Dataset (DTD)

To better understand the peculiarities of MCs' statistical properties, we compare them to a very wide set of everyday textures: the Describable Textures Dataset (DTD) (Cimpoi et al. 2014). This dataset is in open access<sup>17</sup>. In this paper, we keep only the images with smaller edge size larger than 512 pixels. We then crop each one of these  $\sim 1050$  resulting pictures around its center into a  $512 \times 512$  patch. Then each patch is converted to grayscale by summing its three RGB channels. These maps have integer values that range from 0 to  $3 \times 255 = 765$  that we finally divide by a factor  $10^3$  to match the typical values of the other datasets.

<sup>17</sup> <https://www.robots.ox.ac.uk/~vgg/data/dtd/>

## Appendix B: Apodization

The  $256 \times 256$  sub-patches on which we perform 2D Fourier transform do not have periodic boundary conditions (PBC). Thus, before applying such transform during power spectrum estimation on a given sub-patch  $x$ , we first apodize it as follows:

$$x \mapsto rw \cdot (x - \langle x \rangle_w),$$

where  $w$  denotes the pixel-wise multiplication by the window  $w$ , reported in Fig. B.1 and  $r$  is a scalar factor depending on the input map  $x$  such that the output apodized map has same variance as the input. The resulting map does not share the same mean with the input but this property is not regarded by the Fourier-based statistics used here.

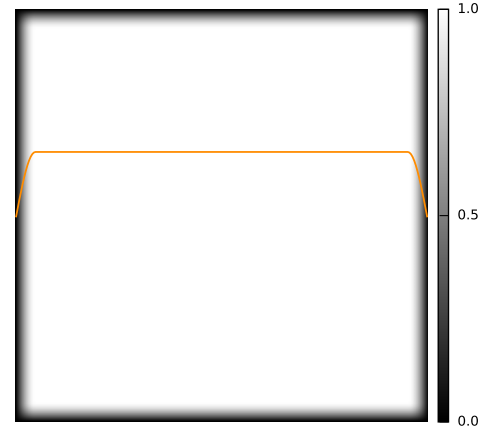


**Fig. B.1.**  $256 \times 256$  apodization window  $w$  used. The orange line is a 1D slice of the middle of the window.

## Appendix C: Srivastava & Du test statistic

The test statistic  $d_\phi^2(x_i, x_j)$  we introduce in Eq. 2 is derived from Srivastava & Du (2008). We apply this test on the two collections of summary statistics  $\{\phi(x_i^{(l)})\}_{1 \leq l \leq N_i}$  and  $\{\phi(x_j^{(l)})\}_{1 \leq l \leq N_j}$  computed on the sub-patches (indexed by  $l$ ) of the patch  $x_i$  and the patch  $x_j$ . In our case,  $N_i = N_j = 4$ . We recall Eq. 2 here:

$$d_\phi^2(x_i, x_j) \equiv \alpha [(\hat{\mu}_i - \hat{\mu}_j)^T D_S^{-1} (\hat{\mu}_i - \hat{\mu}_j) - \beta]. \quad (\text{C.1})$$

This equation is based on the following quantities:

$$\hat{\mu}_i \equiv \langle \phi(x_i^{(l)}) \rangle_{1 \leq l \leq N_i},$$

$$p = \dim \phi, \text{ and } n = N_i + N_j - 2,$$

$$\begin{cases} S_i \equiv \langle [\phi(x_i^{(l)}) - \hat{\mu}_i][\phi(x_i^{(l)}) - \hat{\mu}_i]^T \rangle_{1 \leq l \leq N_i}, \\ S \equiv \frac{1}{n}(N_i S_i + N_j S_j), \\ D_S \equiv \text{diag } S, \end{cases}$$

$$\begin{cases} R \equiv D_S^{-1/2} S D_S^{-1/2}, \\ c_{p,n} := 1 + \text{tr} R^2 / p^{3/2}, \\ \alpha \equiv \frac{N_i N_j}{N_i + N_j} \frac{1}{\sqrt{2(\text{tr} R^2 - p^2/n)c_{p,n}}}, \\ \beta \equiv \frac{N_i + N_j}{N_i N_j} \frac{np}{n-2}. \end{cases}$$

## Appendix D: Why taking the logarithm of some standard statistics?

In theory, because the mapping  $\psi \mapsto \log \psi$  is invertible, the same amount of information should be contained in  $\phi(x)$  and in  $\log \phi(x)$  (when the latter is well defined). However, for the compatibility diagnostic we chose, these two options might perform differently. Such issues are not specific to this test and also occur with standard diagnostics such as Fisher analysis [Park et al. \(2023\)](#).

First, this non-linear mapping can change the fulfillment level of the test assumptions. In the Srivastava & Du test used here, the two input distributions that are to be compared are assumed to be normally distributed and have equal variance. In many cases, typically when  $\phi(x) > 0$ , taking the logarithm of  $\phi(x)$  decreases the deviation to normality and decreases the relative deviations between the variances of  $\phi(x_i)$  and  $\phi(x_j)$ .

Second, this could lead to dramatic improvement in incompatibility detection, as illustrated in Fig. D.1 for  $\phi = \phi_{\text{var}}$  (provided that the assumptions of the test are not too discarded in both cases for these results to be appropriately interpreted).

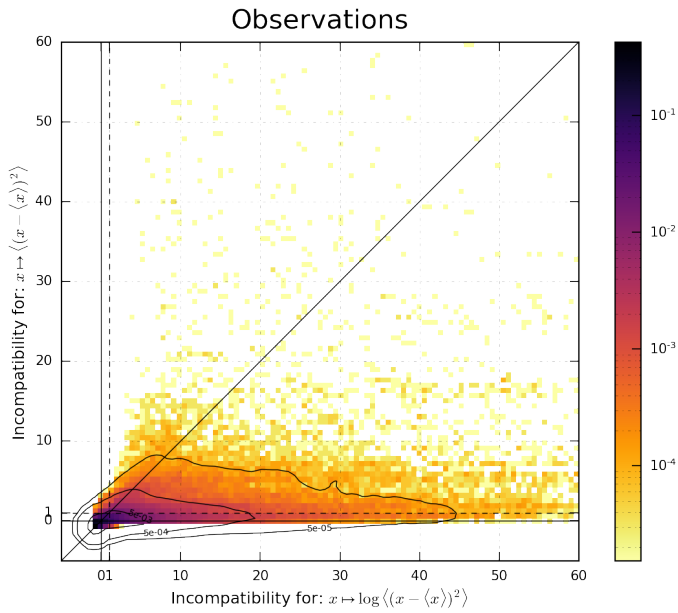


**Fig. D.1.** Effect of the log rescaling after computing variance statistics on observation data. Provided that the assumptions of the test are not too discarded in both cases for these results to be appropriately interpreted on both axes, this shows that  $\langle [x - \langle x \rangle_u]^2 \rangle_u$  is strictly more degenerate than  $\log \langle [x - \langle x \rangle_u]^2 \rangle_u$ .